



# Investigation of mechanisms leading to water drop breakup at Mach 4.4 and Weber numbers above $10^5$

David Hébert<sup>1</sup> · Jean-Luc Rullier<sup>1</sup> · Jean-Marc Chevalier<sup>1</sup> · Isabelle Bertron<sup>1</sup> · Emilien Lescoute<sup>2</sup> · Florent Virost<sup>3</sup> · Hazem El-Rabii<sup>3</sup>

Received: 4 October 2019 / Accepted: 3 December 2019 / Published online: 12 December 2019  
© Springer Nature Switzerland AG 2019

## Abstract

The paper presents an investigation on water drop breakup in the ‘catastrophic’ mode at Weber numbers above  $10^5$ . Experimental data have been obtained on a detonation shock tube operated at a Mach number between 4.2 and 4.6. Displacement and deformation of the mist cloud generated around the droplet were observed with a shadowgraph system, and Schlieren imagery was used to visualise the bow and wake shocks around the droplet. We observe that all measured quantities scale with the initial drop diameter. In order to analyse the experimental results and relate these observables to the breakup process, numerical hydrodynamic simulations have been performed. Once validated by direct comparison with our experimental observations, the simulation results are used to see “through” the mist and infer the droplet evolution with dimensionless time  $T$ . According to our results, the breakup mechanism can be divided into 3 steps. First ( $T < 1$ ), most of the liquid mass remains in one main drop, whose shape flattens due to the hydrodynamic forces; then ( $1 < T < 2$ ) fragmentation begins along the outer rim of the liquid drop and splits the corresponding mass into two parts; the first spreads out radially in small fragments while the remains finally ( $2 < T < 3.5$ ) take the shape of a filament aligned with the flow. Our results are consistent with a complete breakup time  $T_b = 5.5$ .

**Keywords** Breakup · Deformation · Droplet · Catastrophic · Unsteady drag coefficient · Shock stand-off distance

## 1 Introduction

The breakup of liquid sprays exposed to a supersonic flow occurs in many industrial or research applications, such as propulsion (diesel engines [1], rotating detonation engines [2]), blast mitigation [3], and nuclear reactor safety [4]. Due to its importance, abundant work has been done to describe and understand the atomisation process, both experimentally [3] and numerically [5, 6]. The usual macroscopic models describing fluid-spray interaction rely on coupling terms driving the mass, momentum and energy exchange between the liquid and gaseous phase [7]. These coupling terms are directly related to the

drop deformation and fragmentation (or breakup), which dramatically affect the exchange surface between both phases [5, 8].

Due to the difficulty in observing the physical processes occurring at microscale under such conditions, substantial experimental effort has been devoted to the interaction of a single droplet with a supersonic flow, associated with intensive discussion of the numerous physical mechanisms involved (hydrodynamic instabilities, viscous or capillary forces, and thermal effects). Extensive reviews of these studies can be found in the works of Pilch [9], Gelfand [10], Guildenbecher [11] and Theofanous [12], among others. All of these authors agree on classifying the droplet fragmentation into several regimes, primarily

✉ David Hébert, david.hebert@cea.fr | <sup>1</sup>CEA DAM, CESTA, 15 Avenue des Sablières CS60001, 33116 Le Barp Cedex, France. <sup>2</sup>CEA DAM, DIF, 91297 Arpajon Cedex, France. <sup>3</sup>Institut Pprime – UPR 3346 CNRS, ISAE-ENSMA, 86961 Futuroscope Chasseneuil, France.



depending on the Weber number  $W_e$ , defined as the ratio of the disruptive aerodynamic forces to the stabilising capillary force. The traditional description [9, 11] considers the existence of five distinct regimes, which are, by order of increasing  $W_e$ , the vibrational, bag, bag-and-stamen, stripping and catastrophic regimes, with the last one occurring for Weber numbers above 350. More recently, Theofanous [13] studied aerobreakup in rarefied supersonic flows, and proposed a reclassification into two principal breakup regimes: Rayleigh–Taylor Piercing (RTP) and Shear-Induced Entrainment (SIE), the latter being the terminal regime for  $W_e > 10^3$ . When catastrophic/SIE regime conditions are reached, the fluid-droplet interaction generates a micromist [14] cloud, which hides the main shattering drop and limits classical shadowgraph analysis. In order to overcome such a difficulty, improved visualisation techniques have been developed, such as X-ray radiography [15], holographic interferometry [16], and laser-induced fluorescence (LIF) [12]. If we focus on experimental data with water droplets, several studies can be found for  $W_e$  between  $10^3$  and  $10^4$  [12, 16, 17]. However, only a few concern  $W_e$  between  $10^4$  and  $10^5$  [15, 17–19], and even fewer concern  $W_e$  greater than  $10^5$  [15, 19]. Thus, it appears that there is a need for new experimental data to investigate the breakup mechanisms in this regime.

As a complement to the experimental investigations, direct numerical simulation (DNS) has been an active and growing field of research to understand droplet breakup mechanisms, since it allows detailed examination of the fluid-droplet interaction. Various numerical methods have been used with success, such as Volume of Fluid (VOF) [20, 21], and diffuse interface [22]. The major limitation for this approach appears to be the various length scales of the breakup process, from the initial droplet, usually mm size, to the daughter droplets, typically one or two orders of magnitude smaller [4, 23], and even down to the viscous boundary layer around the mother drop at  $\mu\text{m}$  scale [24]. Thus, there are at least four orders of magnitude between the simulation domain and the mesh size, so a minimum of  $10^{12}$  grid points are required for a realistic 3D simulation, and  $10^8$  are required in 2D. Due to their lower computational cost, 2D geometries have been the first used for comprehensive studies [24–27]. 3D simulations have also been performed, with the assumption that viscous or capillary effects are negligible [28]. A second limitation of the simulations comes from the fact that a quantitative comparison with experiments is difficult because much of the experimental data does not provide all of the information on the time and length scales. For instance, many authors [22, 27, 29–31] validate their numerical tools by comparison with 2D experiments performed by Igra [32] or Sembian [33]. Other comparisons remain rather qualitative. Despite these limitations, DNS results have been

used to discuss the transitions between the experimentally observed modes, especially at low  $W_e$  [21]. They also yield access to patterns that are difficult to see experimentally, such as the internal flow field of the drop [34] or the instability growth [24, 28]. Moreover, DNS has been used as a tool to propose other phenomenological descriptions of the breakup. One example is the definition of 3 stages in the breakup process [22], which are namely the raising of a surface wave, the droplet flattening, and the entrainment from the peripheral liquid sheet. In another paper [28], the coupling of all mechanisms has also led to the conclusion that breakup consists in one single stage with simultaneous flattening and stripping of the liquid. It is noteworthy that the same trend is observed in DNS as in the experiments: to date, most DNS studies, if not all, concern Weber numbers below  $10^4$  and studies with  $W_e > 10^3$  are quite sparse [22, 34].

The purpose of this paper is to study the catastrophic/SIE breakup regime and, more specifically, at Weber numbers above  $10^5$ , by using a coupled experimental–DNS approach. Experiments have been performed on a detonation shock tube at a Mach number between 4.2 and 4.6. During each experiment, the droplet was observed with a 16-frame gated camera, using a laser shadowgraph system. Schlieren imagery was used to visualise the supersonic air flow around the droplet and, more specifically, the bow and wake shocks. We will show that these features, which have received little attention in the literature, can provide important additional information on the breakup process. In order to analyse the experimental results, 2D axisymmetric numerical simulations have been performed. Once validated by direct comparison with our experimental observations, we use our DNS results to see “through” the mist and infer the droplet evolution.

The present paper is organised as follows. A precise description of the experimental apparatus is given in Sect. 2, and the experimental results are presented and analysed in Sect. 3. Section 4 describes the numerical tools and the simulation conditions. The DNS results are presented and analysed in Sect. 5, where they are compared to experimental observations. The major conclusions are summarised in Sect. 6.

## 2 Experimental apparatus

The test facility used in this water droplet breakup study is a 92 mm inner diameter detonation-driven shock tube. The use of a detonation in the booster and the driver section increases the pressure and temperature reached relative to a conventional shock tube, and thus allows running at Mach numbers up to 11 [35, 36]. A schematic view of the facility, shown in Fig. 1, indicates the different

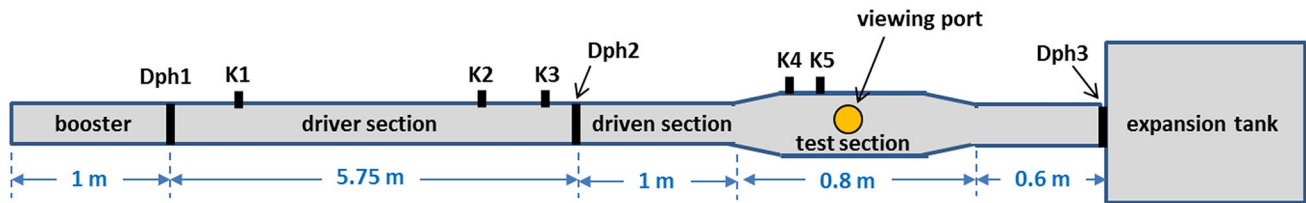


Fig. 1 Schematic diagram of the test facility

sections, separated by a diaphragm (100  $\mu\text{m}$ -thick Mylar membrane, noted as Dph) and the location of the shock-velocity and pressure monitoring components (Kistler 603B, noted as K). For experiments reported in this paper, the booster is pressurised at 1.5 bar with a stoichiometric  $\text{C}_2\text{H}_4\text{-O}_2$  mixture, the driver section is filled at 2 bar with a stoichiometric mixture of hydrogen and oxygen diluted with a 68 vol% or 73 vol% of helium, and the driven section including the test section is filled with air at ambient conditions. These works were strictly controlled before and during injection, in order to ensure good shock wave reproducibility. Ignition is produced in the left closed end by means of an electric igniter; the main wave propagates from left to right. For the tests run with these parameters, the measured Mach number was  $M=4.30\pm 0.10$  using 73% of helium, and a little higher with 68% of helium reaching  $M=4.55\pm 0.10$ . The experimental chamber located at the end of the driven tube is a 0.5 m long segment with a square section of  $80\text{ mm}\times 80\text{ mm}$  and a round/square transition 150 mm long at both sides. This segment is equipped with viewing ports, through which laser shadowgraph or Schlieren photographs are obtained at suitable times for the droplet/shock wave interaction. At the end of the tube, an expansion tank maintains sub-atmospheric pressure, avoiding overpressure for long periods, for window and monitoring component care.

As illustrated in Fig. 2, we use a 527 nm wavelength continuous laser to illuminate the centre of the chamber and to perform a fast visualisation perpendicular to the flow. In order to follow the drop displacement, a sufficiently large zone is illuminated. The viewing ports are BK7 windows flush with the inside wall to minimise flow perturbation. After each run, cleaning was performed and they were changed only if damage was detected. The two Kistler components (K4 and K5) located at 150 mm and 50 mm forward of the drop position provide the front speed that is compared with the shock velocity measured from camera images. The K4 component also provides the initial time for laser and camera triggering. At the test chamber exit, the originally collimated beam passes through two convex lenses whose focal lengths were adapted to the observation region required. The knife-edge located at the focal length of the first lens ( $f_1$ )

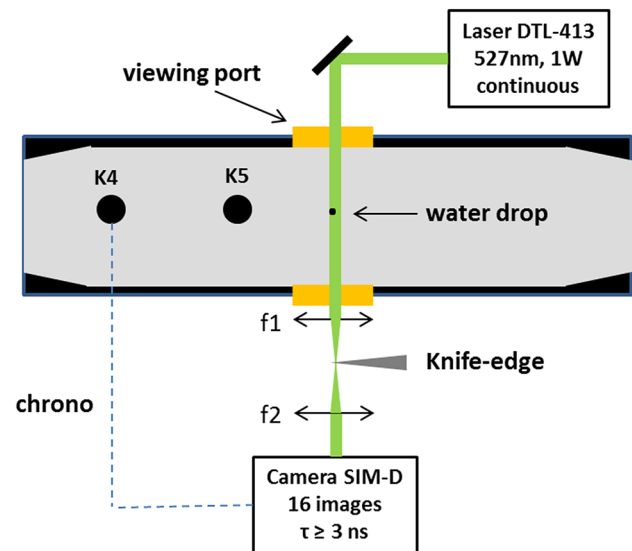
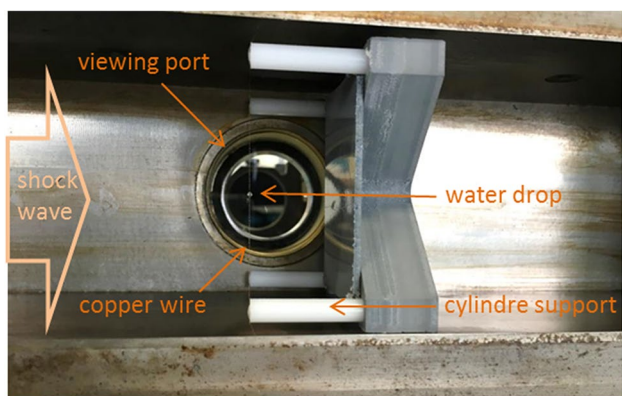


Fig. 2 Schematic diagram of the experiment chamber with associated imaging system (top view)

eliminates the uniform component to obtain Schlieren images of the beam illuminating the CCD of the high-speed camera. The SIM-D camera records 16 images with adjustable frame exposure and delay between two successive images. For the present experiments at a Mach numbers around 4.4, a constant delay of 0.5, 3 or 5  $\mu\text{s}$  was used with 10 ns exposure time.

The experiments were run with a millimetric water drop hung up at the crossing of two copper wires (25  $\mu\text{m}$  of diameter). For all results presented later in this article, the drop/wire diameter ratio is sufficiently high (30 to 50) for no significant wire-induced alteration throughout the drop evolution to be expected. Copper wires were attached to a suitable support, shown in Fig. 3, satisfying the following conditions:

- drop centred on the chamber section with wires parallel to the shock wave plane;
- four white cylinders supporting copper wires positioned at the cavity corners to maximise the delay of the perturbing shock that they will generate;



**Fig. 3** Side photograph of the inner part of the experiment chamber 1 min before the test. It shows all of the elements of the drop holding system: copper wires, white cylinders and supporting rigid structure

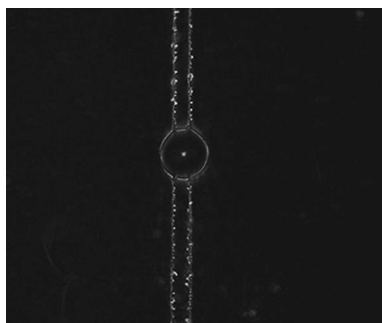


**Fig. 4** Schlieren image of a 1-mm water drop suspended from the two crossed copper wires

- support cylinder length greater than 60 mm, in order to avoid any effect of the rigid structure supporting the white cylinders.

For each test, as shown in the example in Fig. 3, a photograph of the inner part of the experiment chamber was taken just before closing the chamber port and arming the different diagnostic tools. This image remains the only

means to check a parameter after the destructive impact caused by the shock wave.

For accurate measurement of the size of the water drop, a complementary image was obtained before the interaction with the shock wave using a slow, but high-resolution, CCD camera. An example of a millimetre water drop imaged  $\approx 10 \mu\text{s}$  before arrival of the shock wave is shown in Fig. 4. The presence of glue, necessary to hang the drop up on the copper wire, is clearly observed thanks to the increase in contrast from the Schlieren mode. The glue droplet sizes are  $< 20 \mu\text{m}$ , which corresponds to a mass four orders of magnitude smaller than the water drop. Therefore, both the copper wire and glue droplets are considered negligible for the analysis of data presented in the next part. The validity of this assumption will be confirmed throughout this paper by comparison with other experimental results from the literature.

### 3 Experimental results

Experimental studies have been performed on water drop diameters  $\varnothing_d$  ranging from 740 to 1550  $\mu\text{m}$  with a precision of  $\pm 25 \mu\text{m}$ , such as evaluated from camera images. Comparable initial air pressure  $P_0 = 1.013 \text{ bar}$  was used in all of these tests for the test section, and the initial temperature condition ( $T_0$ ) was measured at the filling instant. The corresponding sound velocity ( $C_0$ ) and density ( $\rho_0$ ) of the gas were deduced by considering an air humidity of 1% (dry air). We ran a set of tests at a Mach number of around  $M = 4.4$ , by pressurising the booster at 1.5 bar and the driver section at 2 bar including 68% or 73% of helium for Tests No. 1–4 or Tests No. 5–7, respectively. The set of tests is detailed in Table 1, where the different parameters were obtained by measurements or deduced from elementary equations:

- the Mach number:  $M = V_s / C_0$ , where  $V_s$  is the incident shock speed measured through camera images;

**Table 1** Set of experiments at Mach numbers around 4.4

Test number	$\varnothing$ drop ( $\mu\text{m}$ )	$T_0$ ( $^\circ\text{C}$ )	$C_0$ (m/s)	$\rho_0$ ( $\text{kg}/\text{m}^3$ )	Mach	$V_{m1}$ (m/s)	$P_1$ (bar)	$\rho_1$ ( $\text{kg}/\text{m}^3$ )	$W_e$	$R_e$	$t_c$ ( $\mu\text{s}$ )
No. 1	1550	30	349.2	1.16	4.36	1210	22.48	5.65	$1.78 \times 10^5$	$2.22 \times 10^5$	17.0
No. 2	1135	30	349.2	1.16	4.25	1173	21.30	5.55	$1.20 \times 10^5$	$1.54 \times 10^5$	13.0
No. 3	1280	19	342.8	1.21	4.37	1185	22.44	5.79	$1.45 \times 10^5$	$1.84 \times 10^5$	14.2
No. 4	1130	19	342.8	1.21	4.29	1160	21.62	5.72	$1.21 \times 10^5$	$1.57 \times 10^5$	12.9
No. 5	740	36	352.7	1.14	4.57	1294	24.81	5.77	$0.99 \times 10^5$	$1.15 \times 10^5$	7.5
No. 6	900	36	352.7	1.14	4.59	1299	24.97	5.78	$1.22 \times 10^5$	$1.41 \times 10^5$	9.1
No. 7	850	36	352.7	1.14	4.51	1272	24.08	5.71	$1.09 \times 10^5$	$1.29 \times 10^5$	8.8

- the matter velocity:  $V_{m1} = a V_s - b$ , where the coefficients  $a = 0.943$  and  $b = 227$  are taken from [37] to account for real gas effects;
- the matter pressure:  $P_1 = P_0 + \rho_0 V_s V_{m1}$  (Rankine–Hugoniot formula [38]);
- the matter density:  $\rho_1 = \rho_0 V_s / (V_s - V_{m1})$  (Rankine–Hugoniot formula [38]);
- the Weber number:  $W_e = \rho_1 V_{m1}^2 \varnothing_d / \sigma$ , where  $\sigma = 0.072$  N/m is the water surface tension;
- the Reynolds number:  $R_e = \rho_1 V_{m1} \varnothing_d / \mu_1$ , where  $\mu_1 = \mu_0 f(T_0, T_1)$  is the air viscosity defined by the Sutherland formula [39] ( $\mu_0 = 1.79 \times 10^{-5}$  N/m/s being the air viscosity at ambient temperature);
- the Rayleigh time:  $t_c = \varnothing_d (\rho_d / \rho_1)^{1/2} / V_{m1}$ , where  $\rho_d = 1000$  kg/m<sup>3</sup> is the water drop density.

The choices for the size of the visualisation frame and the delay between two images were not the same for all tests, which allowed us to conduct various investigations of the results. In the following we analyse the seven tests of our experiment with a chronological time evolution intending to separate different steps of water drop break-up.

Previous works [4, 40] have revealed that the characteristic time and length scale for describing break-up evolution are the Rayleigh time  $t_c$  and the initial drop diameter  $\varnothing_d$ . Thus, we define the dimensionless time  $T$  as  $T = t/t_c$  and the dimensionless distance  $D = d/\varnothing_d$ .

### 3.1 Stripping/SIE initiation: $T < 0.5$

Test No. 1 is focused on early times of drop-flow interaction. Thus, a short inter frame delay of  $0.5 \mu\text{s}$  and a strong magnification of  $1.94 \mu\text{m}/\text{pixel}$  (area of  $2.47 \times 1.85 \text{ mm}^2$ ) have been selected for this test, as shown in Fig. 5. With these parameters, the generation of a micromist at the periphery of the droplet is clearly identified immediately after the shock wave passage over the drop. These images are very similar to those defining the so-called stripping regime [13, 16, 23] or SIE [12]. Simultaneously, the bow shock formation is observed in Fig. 5. The dimensionless time mentioned for each image suggests a beginning of the stripping mechanism at  $T \leq 0.1$ . To our knowledge, such observations at  $W_e > 1.7 \times 10^5$  and  $R_e > 2.2 \times 10^5$  have never been mentioned before in the literature.

### 3.2 Repeatability: $0 < T < 1.6$

The two following tests were run with a small difference between parameters. A comparison of Tests No. 2 (blue) and No. 3 (green) is shown in Fig. 6, where the dimensionless time is mentioned for each image. Identical camera parameters were also chosen, including a  $16.75 \times 12.57 \text{ mm}^2$  area per image and a delay of  $3.0 \mu\text{s}$  between two successive images. With regard to the complexity of such an experiment, a very satisfying reproducibility is observed. The leading edge of the mist cloud, as well as the bow and wake shocks, follow equivalent progress throughout the sequence of Schlieren images. Although light differs slightly between the two tests, the mist (black area around the drop) and its associated turbulence (resembling a tail behind the mist)

**Fig. 5** Shadowgraphs of a  $1550 \mu\text{m}$  water drop at the beginning of the interaction ( $M = 4.36$ ,  $W_e = 1.78 \times 10^5$ ,  $R_e = 2.22 \times 10^5$ ), showing the beginning of stripping at the equator of the droplet a very short time after the passing of the incident shock wave. Also shown are the copper wires holding the droplet and the bow shock due to the supersonic flow around it

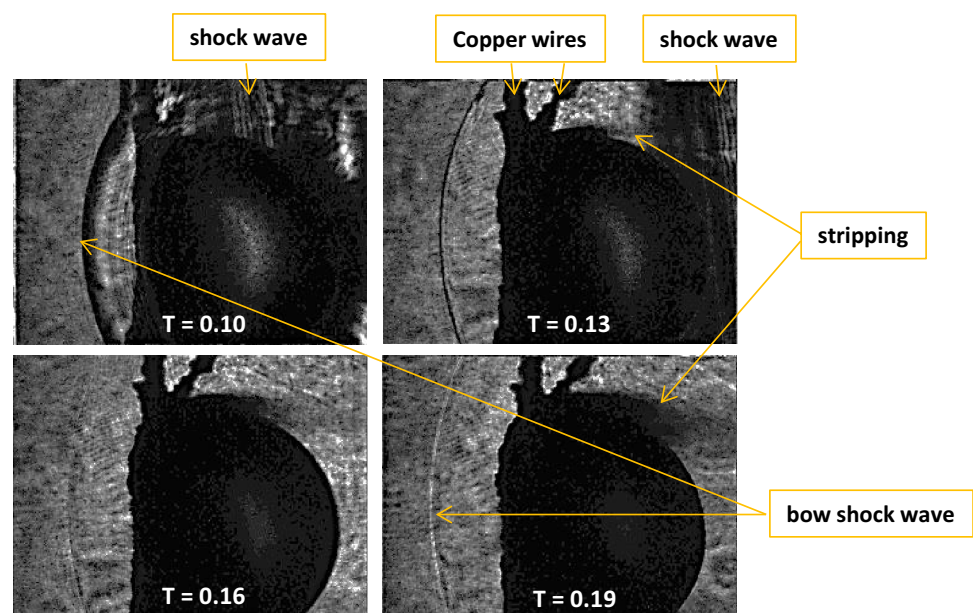
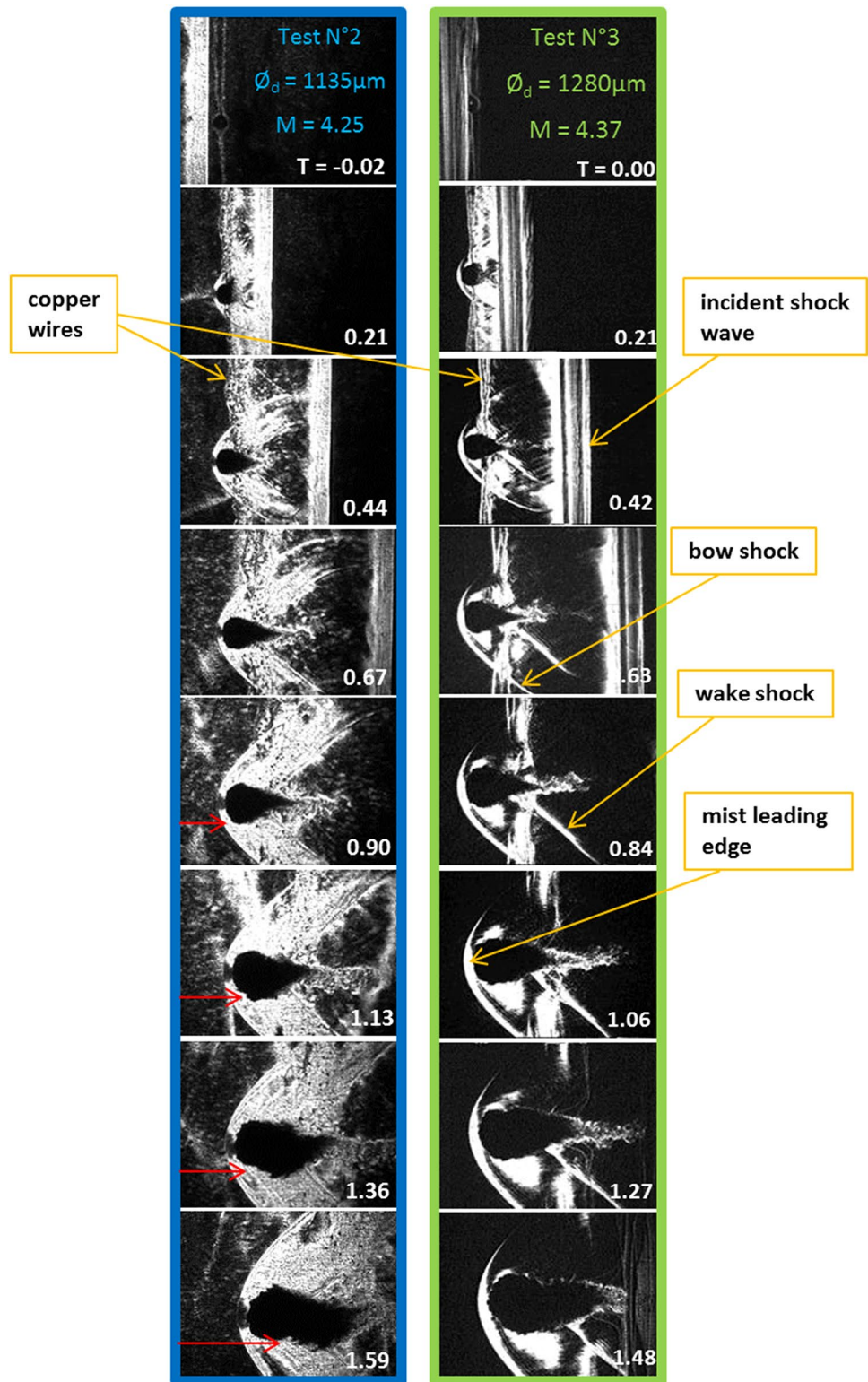


**Fig. 6** Schlieren images of two comparable tests with similar initial conditions and camera parameters. The red arrows indicate the separation of a probable cluster of fragments for Test No. 2. The yellow arrows indicate various patterns whose evolutions can be observed and compared in the two image sequences



grow at the same speed, generating comparable shapes. We also observe that copper wires move farther than the drop and cross the mist without substantially modifying its shape, as expected from the wire size. For both cases, it is notable that at  $T > 1$  the mist containing the drop has partially lost

its axial symmetry, and the two last images ( $T \approx 1.5$ ) show that a portion of the mist seems to have become detached from the main part moving farther. More accurately, the red arrow indicates for Test No. 2 the separation of a fragment (or a cluster of fragments) between  $T = 0.9$  and  $T = 1.13$ . The

latter moves faster than the main drop and also generates mist and a secondary fragment, as can be seen in two succeeding images.

The whole drop and mist are no longer visible in the following images of Fig. 6 (i.e., at  $T > 1.6$ ), but the windward portion is still observable and allows us to estimate some parameters that characterise the interaction of a liquid drop with a supersonic air flow. These are the drop displacement, its transverse deformation, the standoff distance of the bow shock from the mist leading edge, and the distance between the bow and wake shocks.

### 3.3 Drop displacement: $0 < T < 3.5$

Previous works have revealed that drop acceleration is the dominant parameter governing drop break-up [9]. However, the drop displacement associated with the centre of mass motion is not accessible experimentally because of the mist surrounding the drop. The usual approach relating to drop displacement does not reflect the complicated influence of drop deformation, mass loss and break-up. The drop is typically modelled as a rigid sphere of constant mass, neglecting its velocity relative to the free stream velocity and the presence of a surrounding mist. Based on these assumptions, the equation governing the centre of mass displacement  $x$  is:

$$m \frac{d^2x}{dt^2} = \frac{1}{2} C_d \cdot \rho_1 \cdot A \cdot V_{m1}^2$$

where  $C_d$  is the drag coefficient. In the case of a sphere of diameter  $\varnothing_d$ , and density  $\rho_d$  the ratio of its mass  $m$  to its cross area  $A$  is:

$$\frac{m}{A} = \frac{2}{3} \varnothing_d \cdot \rho_d$$

and the previous equation becomes:

$$\frac{\rho_d}{\rho_1} \cdot \frac{\varnothing_d^2}{V_{m1}^2} \cdot \frac{1}{\varnothing_d} \cdot \frac{d^2x}{dt^2} = \frac{3}{4} C_d$$

where we recognize the characteristic Rayleigh time  $t_c$ :

$$\frac{t_c^2}{\varnothing_d} \cdot \frac{d^2x}{dt^2} = \frac{d^2X}{dT^2} = \frac{3}{4} C_d$$

Finally, as long as its relative velocity is small, the rigid sphere will undergo constant acceleration and its dimensionless equation of motion is:

$$X = \frac{x}{\varnothing_d} = \frac{3}{8} C_d T^2 \tag{1}$$

Similarly, the instantaneous dimensionless drop displacement is commonly presented in the literature by Eq. (1), where  $x$  is the measured displacement of the mist leading edge (MLE) and not of the centre of mass. In this case, the drag coefficient  $C_d$  describes the complicated influences of drop deformation, mass loss and early break-up. This coefficient is obtained by performing a curve fit to  $x = f(t)$  assimilated as the drop displacement. The displacement data obtained from our experiments are plotted in Fig. 7a, displaying the difference between the two percentages of helium in the driven section, together with the good reproducibility of our experimental facility. Thus, the data of Tests No. 1 to No. 4 show similar curves corresponding to a Mach number of around 4.30 and, likewise, the data of Tests No. 5 to No. 7 show curves corresponding to a Mach number close to 4.55. The drop acceleration is higher for the latter tests, but this difference disappears if we plot the same data using dimensionless time and displacement, as shown in Fig. 7b. The curve fit of our data using Eq. (1) yields a drag coefficient  $C_d = 2.15 \pm 0.05$  with remarkable agreement up to  $T = 3$ .

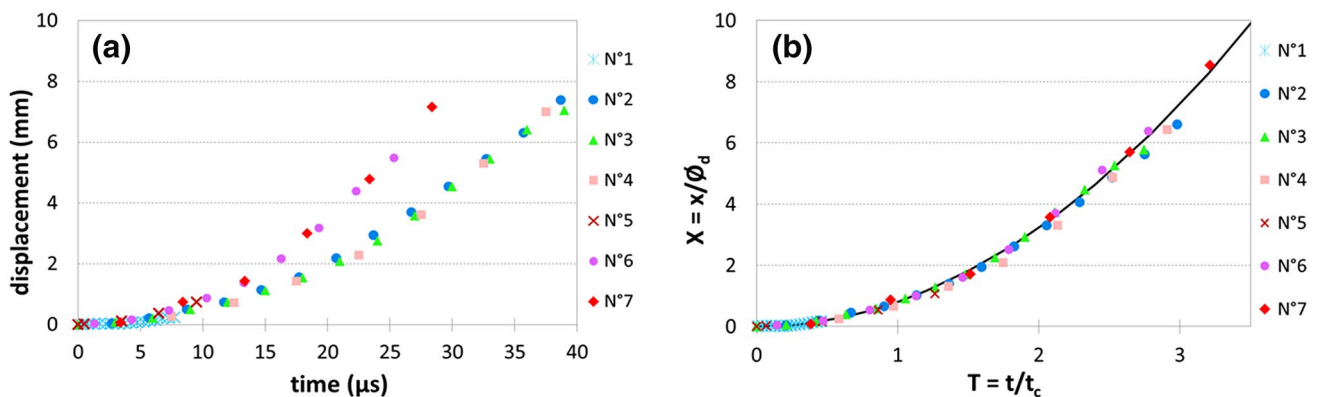
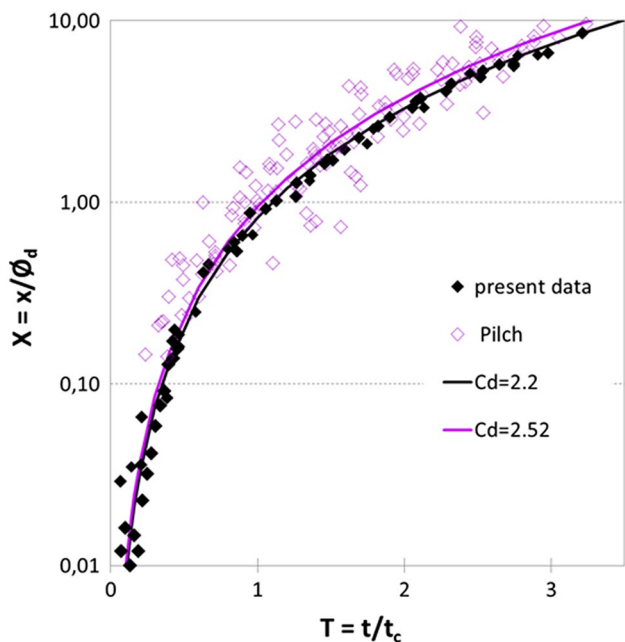


Fig. 7 Drop displacement (a) and dimensionless drop displacement (b) for our complete set of tests. The solid line corresponds to Eq. (1) with  $C_d = 2.15$  (best fit to our data)

To directly compare our results with the previously reported drag coefficient, we have plotted in Fig. 8 the dimensionless displacement in log scale and compared it with data taken from the literature [9], where most works prior to 1981 are shown. The least squares curve fit performed by Pilch on this data set with Eq. (1) yielded an average drag coefficient of 2.52, which is close to our result. In our experiments performed at around  $M=4.4$  with weak parameter variations, much less dispersion is observed and a more precise value has been found for  $C_d$ . As mentioned above, the data labelled ‘Pilch’ in Fig. 8 is a compilation of the data obtained by various authors using different experimental conditions (including set-up, liquid material and diagnostics), which can explain the scatter in the measurements. Also, the large range of Mach, Reynolds and Weber numbers included in this collection may be source of additional dispersion. Therefore, the precise value that we found suggests that the drag coefficient could be related more precisely to some parameters having yet to be established. Moreover, the good agreement between our results and the previous ones can be considered as a validation that the copper wires in our experiments have negligible effect on drop displacement.

### 3.4 Drop deformation: $0 < T < 3.5$

It is established that, when the Weber number exceeds 350, a portion of the mist generated by wave crest



**Fig. 8** Comparison of our experimental data with literature data provided by [9]. The solid line corresponds to Eq. (1) with  $C_d=2.52$  (average value identified by [9])

stripping or SIE is swept out radially [9, 12] and surrounds the liquid core. Therefore, the mist cloud radial extension can be much larger than the real drop and makes the actual droplet deformation very difficult to observe. Despite this ambiguity, the term “drop deformation” has been commonly used to describe what actually corresponds to the mist cloud dimension normal to the gas flow, noted as  $y$  [9, 15]. For consistency purposes, we will use the same definition and, as in the previous sections, we introduce the dimensionless deformation as  $Y = y/\phi_d$ .

However, some ambiguity persists in the measurement of  $y$ , as illustrated by the red arrows in Fig. 9. At early times  $T \leq 1$ ,  $y$  is defined as the maximum lateral dimension of the mist cloud. Then, as already noticed in Sect. 3.2, at times  $T \geq 1.13$  the cloud mist loses symmetry due to some fragmentation. Thus, we choose to adapt the definition of  $y$ . In that way,  $y$  is measured in the front zone, where the axial symmetry is roughly preserved. Then, as a tip appears at the MLE, as observed at  $T = 1.59$ , two values of  $y$  have been reported. Once the dissymmetry becomes too significant ( $T = 2.06$ ) we stop following the larger  $y$ , and the maximum lateral dimension of the tip becomes the new definition of  $y$ . We will show later that this behaviour is an indication of the actual deformation of the remaining liquid core.

Drop deformation is plotted as a function of time in Fig. 10a. It shows the result of our experiments, except Test No. 1 for which the visualisation dimension was too small. The choice of experimental set-up and camera parameters for Tests No. 5 and No. 6 do not permit us to reach the break of the growth observed after a time in the range [12–25  $\mu$ s]. This rupture, associated with the “tip” formation, is regrouped around  $T = 1.5$  when using dimensionless time and deformation, as shown in Fig. 10b. Our measurements are then compared in Fig. 11 with data taken from the literature [9]. Note that we restricted this comparison to data and to a time range where the definition of droplet deformation is not ambiguous (no tip, no symmetry loss, and no limitation by the camera field of view). It appears that our results are consistent with previous works, suggesting again that our holding system with the copper wires does not have a significant effect on the deformation. The drop deformation models of Burgers and Reinecke [41] are also shown in Fig. 11, the latter being a modification of the former in order to improve agreement with experimental observations of the mist cloud lateral expansion. A good agreement is observed with the data up to  $T = 1.5$ . After this time, both models overestimate the experimental observations, which may be attributed to the fact that those models rely on two major hypotheses: (1) that no fragmentation occurs, and (2) that the liquid core deformation can be considered as a global flattening. These two hypotheses thus may not be valid for times  $T > 1.5$ . This is almost certain for the first one, since



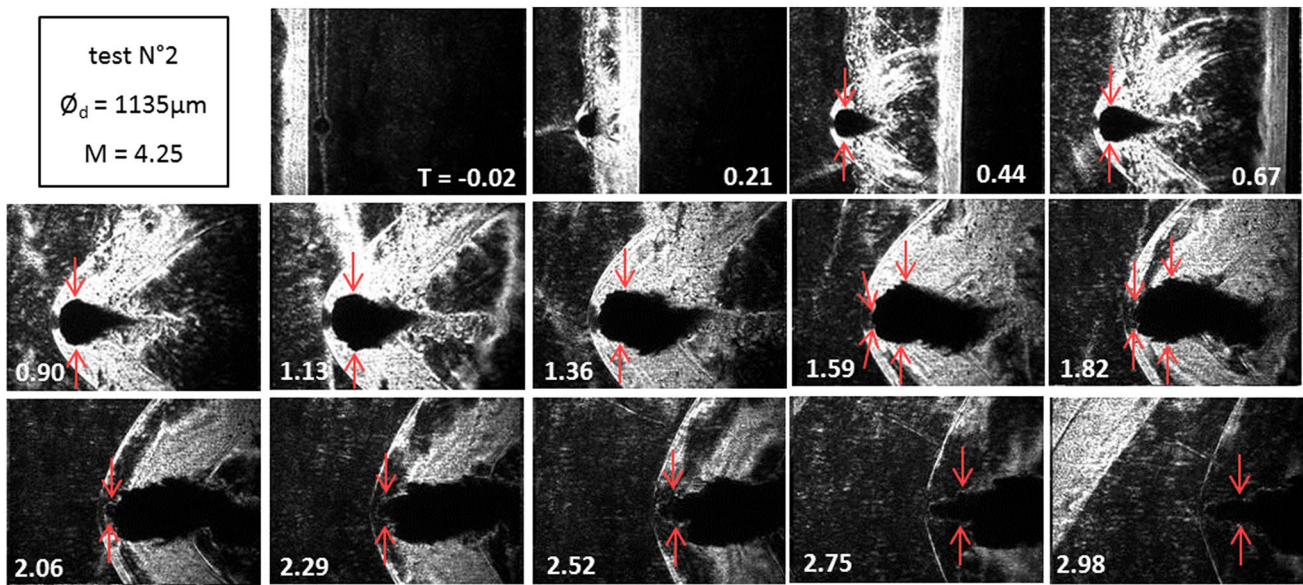


Fig. 9 Schlieren images of Test No. 2, including  $T > 1.5$ . The red arrows show how the drop deformation  $y$  is defined in the present paper

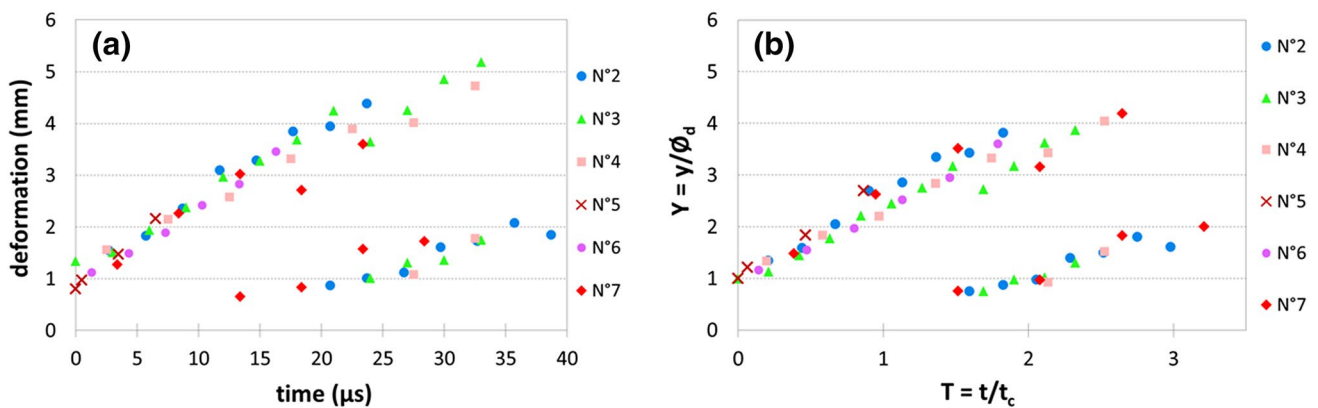


Fig. 10 Drop deformation (a) and dimensionless drop deformation (b) for our set of tests

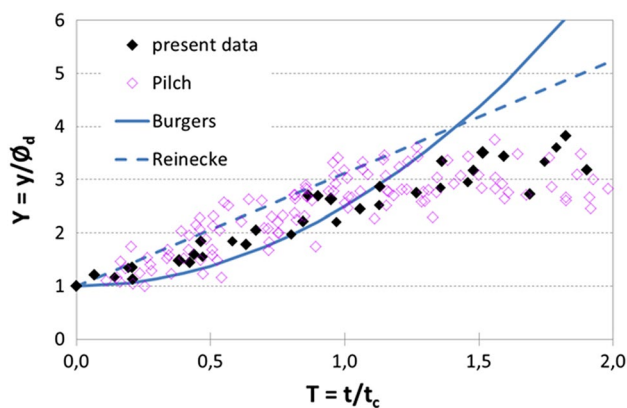


Fig. 11 Comparison of our experimental data with literature data provided by Pilch [9] (synthesis of most works prior to 1981 such that  $1.3 \times 10^3 \leq W_e \leq 1.1 \times 10^5$ ) and with the Burgers and Reinecke models [41]

fragmentation has been observed for Test No. 2 in Fig. 6 at  $T$  between 1.1 and 1.6. Regarding the second hypothesis, we point out that the small tip appears at the mist leading edge, precisely at around  $T = 1.5$ . It is noteworthy that the dimensionless plot in Fig. 10b provides efficient rescaling, even for the tip evolution. This suggests the occurrence of a significant and repeatable hydrodynamic phenomenon and that the liquid core deformation is more complex than the assumptions made by Burgers and Reinecke.

### 3.5 Bow shock standoff distance: $0 < T < 3.5$

Noting as  $b$  the distance from the bow shock to the MLE, we define  $B = b/\phi_d$  as the dimensionless shock layer thickness. From our experiment we present in Fig. 12a the detached shock thickness as a function of time. Test No. 1

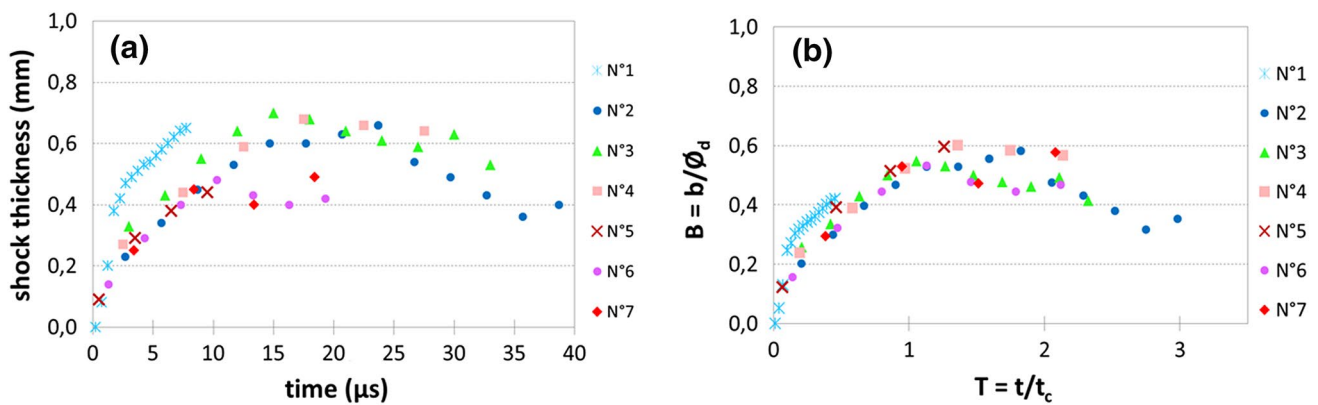


Fig. 12 Shock thickness (a) and dimensionless shock thickness (b) for our set of tests

run with the largest drop is clearly above all others tests, and Tests No. 5 and No. 6 having a upper Mach  $M=4.55$  reach a maximum value at  $t=10\ \mu\text{s}$  instead of  $15\ \mu\text{s}$  for Tests No. 2–4 with  $M=4.30$ . However, plotting these data using dimensionless time and bow shock thickness, we observe in Fig. 12b that all tests have a similar behaviour. At early times, the increase of  $B$  can be interpreted as a signature of the actual liquid core deformation. Indeed, the droplet acts as a blunt body and it has been shown [42] that under such conditions the bow shock standoff distance is directly related to the drop radius and to the relative velocity between the flow and the drop stagnation point. Thus, the increase of  $B$  can be attributed to two simultaneous phenomena, which are (1) the increase of drop apparent diameter due to liquid core deformation and (2) the decrease of relative velocity due to drop acceleration. At later times, dimensionless data show a remarkable stabilisation of the shock layer thickness around  $T=1$ , followed by the maintaining of an approximate constant value  $B$  ranging from 0.5 to 0.6. This rupture in the growth could be attributed to the earliest fragmentation of the flattened drop rim. Such a hypothesis is in good agreement with the above mentioned (red arrows in Fig. 6) discernable generation of fragments between  $T=0.9$  and  $T=1.13$  for Test No. 2. It is important to keep in mind that the measured thickness is the distance between the detached shock and the beginning of the mist (MLE), which may not correspond to the drop edge.

### 3.6 Spacing between bow and wake shock

For each image of the tests, the spacing between the bow and wake shocks, noted as  $w$ , has been measured at a fixed distance from the symmetry axis. This distance cannot be too small, in order to avoid obscuring by the mist cloud. It cannot be too large either, because the shocks could not be observed at early or late times. As a good compromise

for this distance, we choose 5 initial drop radii, as illustrated for Test No. 2 by the red arrows in Fig. 13.

The top and bottom measurements of  $w$  are very similar, and follow the same evolution, suggesting that the air flow around the drop remains roughly symmetrical throughout the entire experiment, even with deformation and fragmentation. When a small difference is observed ( $\leq 10\%$ ) at  $T > 1$ , it can be related to the dissymmetry of the deformation  $y$  mentioned in Sect. 3.4. Then, the average value has been used for comparison between different tests, as shown in Fig. 14a. We observe a continuous increase with a slight difference correlated to the drop size, the largest drop  $\phi_d=1280\ \mu\text{m}$  producing the greatest slope (Test No. 3) and the smallest  $\phi_d=850\ \mu\text{m}$  making the lowest (Test No. 7). As for other parameters that characterise the drop interaction with the air flow, we define the dimensionless distance between the bow and wake shock value by  $W=w/\phi_d$ . Then, the differences of  $w$  between all shots disappear entirely if we use the dimensionless scales, as shown in Fig. 14b.

## 4 Numerical tools and simulations

The major observables in our experiments are the drop displacement, deformation and the shock waves in the surrounding air. These observations suggest that drag forces acting on the drop surface drive its motion and the latter, through droplet displacement and deformation, modifies the air flow. Therefore, it appears that aerodynamics and hydrodynamics need to be strongly coupled in the simulation. The purpose of this section is to describe the numerical tools that we used to solve the aerodynamics (drag forces) and hydrodynamics (fluid motion) consistently, with a non-stationary multi-fluid compressible flow numerical solver (hydrocode). The hydrodynamic phenomenon addressed in the simulation

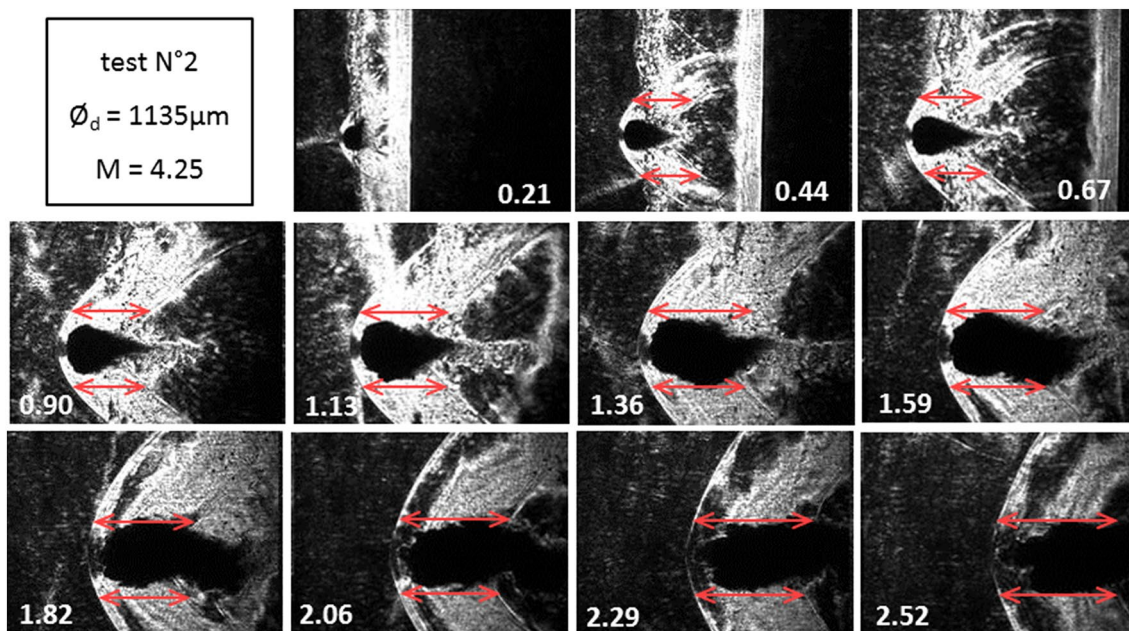


Fig. 13 Schlieren images of Test No. 2. The red arrows show how the distance between the bow and wake shocks  $w$  is defined in the present paper

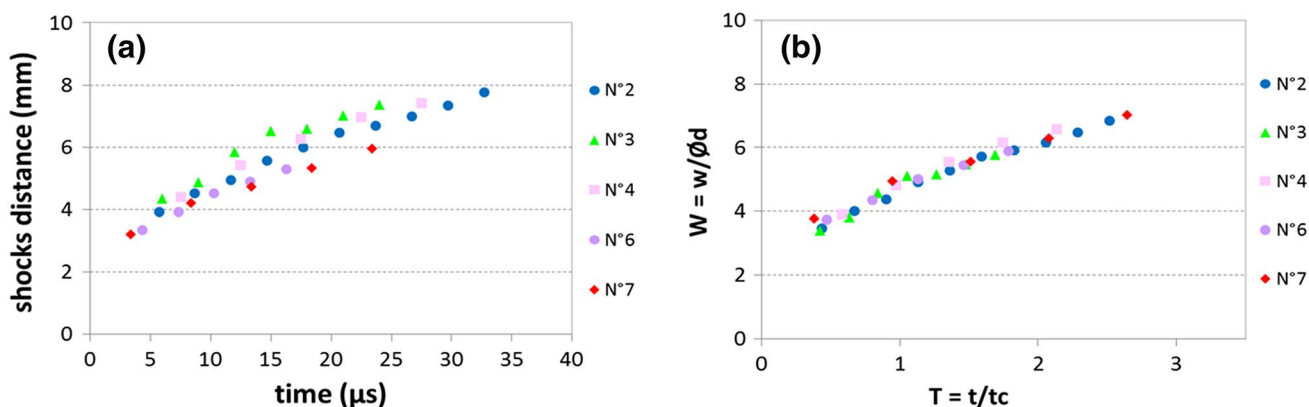


Fig. 14 Distance between bow and wake shocks (a) and dimensionless distance between bow and wake shocks (b) for our set of tests

will thus be the global non-stationary two-fluid flow, including drag forces, shock waves, drop displacement and drop deformation.

### 4.1 Presentation of the simulations

Hydrodynamic simulations have been performed with Hésione, a code developed at the CEA that solves the Euler equations in a 1D, 2D or 3D geometry [43]. These equations (conservation of mass, momentum and energy) are [38]:

$$\frac{\partial \rho}{\partial t} + \nabla \cdot (\rho \mathbf{V}) = 0$$

$$\frac{\partial \mathbf{V}}{\partial t} + \mathbf{V} \cdot \nabla \mathbf{V} + \frac{1}{\rho} \nabla P = 0$$

$$\frac{\partial}{\partial t} \left( \rho E + \frac{\rho \mathbf{V}^2}{2} \right) + \nabla \cdot \left[ \rho \mathbf{V} \left( E + \frac{\mathbf{V}^2}{2} \right) + P \mathbf{V} \right] = 0$$

where  $\mathbf{V}$  is the velocity vector. The closure relation of this system is provided by the material properties. More

**Fig. 15** Schematic diagram of the simulation initial and boundary conditions, showing the air domain split into two zones (in red and blue) and the water drop (in black)

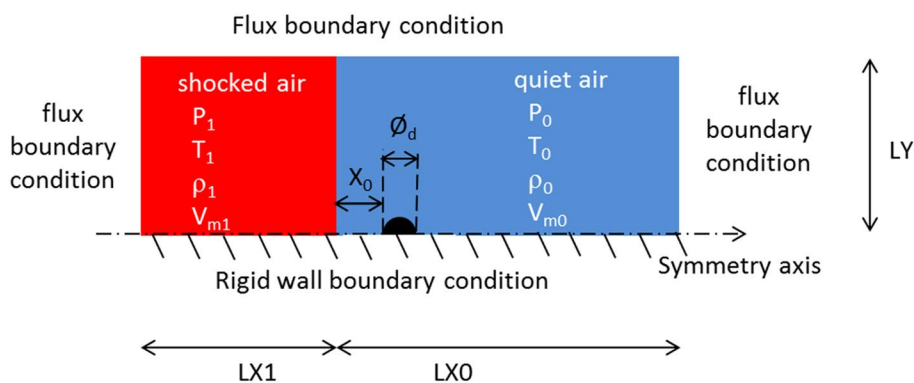


**Table 2** Parameter initial values used in simulations

	$P_i$ (Pa)	$T_i$ (K)	$\rho_i$ (kg/m <sup>3</sup> )	$V_{mi}$ (m/s)	$C_i$ (m/s)	$V_s$ (m/s)	Mach
Water (i=d)	$1.000 \times 10^5$	310	1000	0	1700		
quiet air (i=0)	$1.020 \times 10^5$	315	1.16	0	348		
shocked air (i=1)	$21.10 \times 10^5$	1270	5.71	1175	717	1474	4.24

precisely, pressure  $P$ , density  $\rho$  and specific internal energy  $E$  are consistently calculated by means of an equation of state (EOS). Note that the above equations do not include capillary, viscous nor heat conduction effects. The validity of these equations for our study will be discussed further in Sect. 4.3.

In this study, we used a 2D Cartesian mesh with axial symmetry. The Eulerian solver was used, which in fact consists in a Lagrangian step (i.e., where the mesh follows the matter) using a Godunov scheme [44], followed by the projection of the deformed mesh on the fixed grid. In the case of multi-material flows, it is possible for different fluids to be present in the same cell, where they are represented by their volumic fraction. This is a classical Volume of Fluid (VOF) method, where Mosso’s algorithm [45] is used for interface reconstruction. We assume that all materials within the same cell have the same material velocity, but are not necessarily at the same pressure. A closure relation is used to compute average pressure inside such a cell. In order to solve the 3 above equations, the EOS of each material is required. For water, we used the Zamyshlyayev EOS [46], which is accurate over a wide range of thermodynamic conditions. For air, we used the SESAME 5030 table [47], which includes vibration, dissociation and ionisation. This choice will be discussed further in Sect. 4.2.

The initial and boundary conditions of the simulations are defined in Fig. 15. They are chosen to avoid simulating the whole shock tube, by splitting the air domain into two zones labelled as zero and one, corresponding to quiescent air and shocked air, respectively. To ensure consistency, the initial density ( $\rho_0$ ) and temperature ( $T_0$ ) of quiet air are finely tuned so that the SESAME 5030 EOS provides values for the pressure  $P_0$  and sound speed  $c_0$  close to the

**Table 3** Geometrical dimension data used in simulations

$LX_0$ (mm)	$LX_1$ (mm)	$LY$ (mm)	$\phi_d$ (mm)	$X_0$ (mm)
20.5	1.5	10	1.135	0.5

experimental data. Using these values and the Hugoniot relations, SESAME 5030 EOS provides the shocked air properties ( $P_1, \rho_1, T_1$  and  $c_1$ ). All consistent values are listed in Table 2. They have been chosen to be as close as possible to the experimental Test No. 2 (see Table 1), as well as the geometrical dimensions  $\phi_d$  and  $X_0$  reported in Table 3. The agreement between the physical conditions of our simulation and those of Experiment No. 2 is better than 1%. Other geometrical dimensions are given in Table 3: the length  $LX_1$  of the initial shocked zone is chosen so that the flow interaction with the drop and the subsequent detached shock do not reach the left boundary. Similarly, the upper boundary of the simulation box is not physical. The height  $LY$  has thus been chosen so that the reflected wave due to the interaction of the detached shock with this boundary does not affect the flow in the region of interest.

The present study has been conducted with a 12.5  $\mu\text{m}$  cell size, which corresponds to more than 90 grid points per initial drop diameter. This choice will be discussed further in Sect. 4.3.

#### 4.2 Physical validity of the simulations: EOS of air

In this section we show that a perfect gas EOS for air (i.e., with constant polytropic coefficient) would not be sufficient under the present conditions and that the 5030 SESAME table will be more accurate. We show in Fig. 16 a

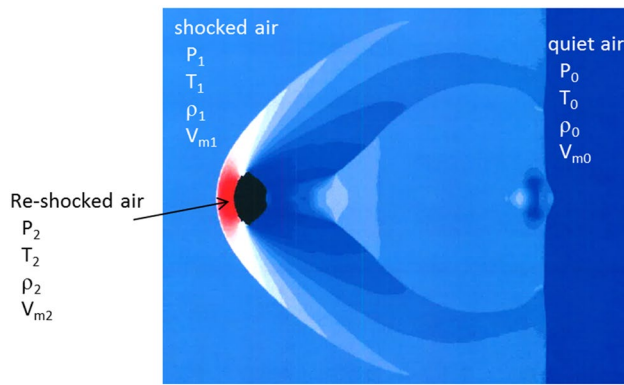


**Fig. 16** Pressure field extracted from the simulation at dimensionless time  $T=0.44$ , around the water drop (in black), emphasising the initial, shocked and re-shocked states of air

quick overview of the physical conditions to which the air is subjected. Under the present experimental conditions, the thermodynamic path of air does not follow a single Hugoniot. Indeed, after being accelerated by the plane shock wave travelling at  $M \sim 4.4$  (after which the pressure  $P_1$  is close to  $2 \times 10^6$  Pa), the air experiences a second shock (the so-called bow shock) due to its sudden deceleration in the vicinity of the droplet, then reaching pressures  $P_2$  above  $7.6 \times 10^6$  Pa.

In order to validate our EOS in the shocked state ( $i=1$  in Fig. 16), we have checked that the 5030 SESAME EOS is consistent with the relation used for experimental analysis in Sect. 3 [37]. The comparison is shown in Fig. 17a, also including the perfect gas EOS with a polytropic coefficient value of 1.4. It appears that all models are very close for a material velocity  $V_{m1}$  between 1100 and 1300 m/s, which corresponds to the shock state ( $i=1$ ) in the experiments discussed here. Some limitations of the perfect gas EOS appear clearly for material velocities exceeding 1500 m/s, which is not the case of the SESAME EOS.

If we now consider the re-shock state ( $i=2$  in Fig. 16), Kim's correlation can no longer be used, but we can still compare the SESAME and perfect gas EOS. Figure 17b shows that they are in good agreement as regards the pressure. However, as shown in Fig. 17c, a difference in density of almost 10% can be observed between both EOS in the re-shocked state. We also note that increasing the value of the Mach number would even decrease the validity of the perfect gas model.

### 4.3 Numerical validity of the simulations: mesh size

A limitation of the Hesione simulations is the absence of any capillary, viscous or thermal effect. The purpose of the present discussion is to assess to what extent these limitations affect the validity of our simulations,

which are limited to purely hydrodynamic effects. We first notice that the two characteristic lengths of our simulations are the drop size ( $\sim 1$  mm) and the mesh size ( $12.5 \mu\text{m}$ ), which are related to the two characteristic times, the Rayleigh time ( $\sim 10 \mu\text{s}$ ) and the hydrodynamic time step ( $\sim 10$  ns), respectively.

Let us now consider the surface tension  $\sigma$ . Capillary forces are comparable to the aerodynamic forces for structures having a radius of curvature  $r_1$  such that  $\rho_1 \cdot V_{m1}^2 \sim \frac{\sigma}{2r_1}$ ; i.e., where the "local" Weber number is of the order of one. Using  $\sigma=0.07$  N/m we find a characteristic length  $r_1 < 10$  nm that is three orders of magnitude below the mesh size used in the simulations. Thus, for all structures of size greater than a few cells, capillary effects are actually negligible.

Regarding viscous effects, they are comparable to the aerodynamic forces for structures having a local velocity gradient  $\frac{V_{m1}}{r_2}$ , such that  $\mu \frac{V_{m1}}{r_2} \sim \rho_1 \cdot V_{m1}^2$ ; i.e., where the "local" Reynolds number is of the order of one. This defines the characteristic length  $r_2 \sim \frac{\mu}{\rho_1 \cdot V_{m1}}$ . Using  $\mu \sim 10^{-3}$  kg/m/s for water leads to  $r_2 \sim 150$  nm, which is two orders of magnitude below the mesh size used in the simulations. Thus, for all structures of a size greater than a few cells, the velocity gradients are sufficiently low to make viscous forces negligible.

To estimate the characteristic scales of thermal effects, we consider that the temperature is imposed at the drop surface. Under such conditions, the thermal conduction problem satisfies the Fourier equation and the characteristic length  $r_3$ , affected by the outer temperature during time  $t_c$ , is  $r_3 \sim \sqrt{\frac{\lambda \cdot t_c}{\rho_d \cdot C_p}}$ , where  $\lambda=0.5$  W/m/K is the thermal conductivity of water,  $C_p=4180$  J/kg/K is its specific heat, and  $\rho_d=1000$  kg/m<sup>3</sup> is its density. Thus, considering the characteristic time for hydrodynamic phenomena  $t_c \sim 10 \mu\text{s}$ , we find  $r_3 \sim 1 \mu\text{m}$ , which is one order of magnitude below the mesh size used in the simulations.

Moreover, it is important to emphasise that no fragmentation model is present in the simulation, and that all of the observed fragmentation will be purely numerical. For all of these reasons, the simulations are expected to be valid as long as we only consider purely hydrodynamic effects at sufficiently large scales (a few tens of  $\mu\text{m}$ ). Keeping this in mind, the analysis of the simulations will focus on "macroscopic" features, at scales similar to those of the experimental data shown in Sect. 3. It is thus pointed out that the simulations are not intended here to resolve scales smaller than those of the experimental observations. Rather, our simulations are expected to be a useful tool to analyse the macroscopic features of experimental data more deeply, yielding access to

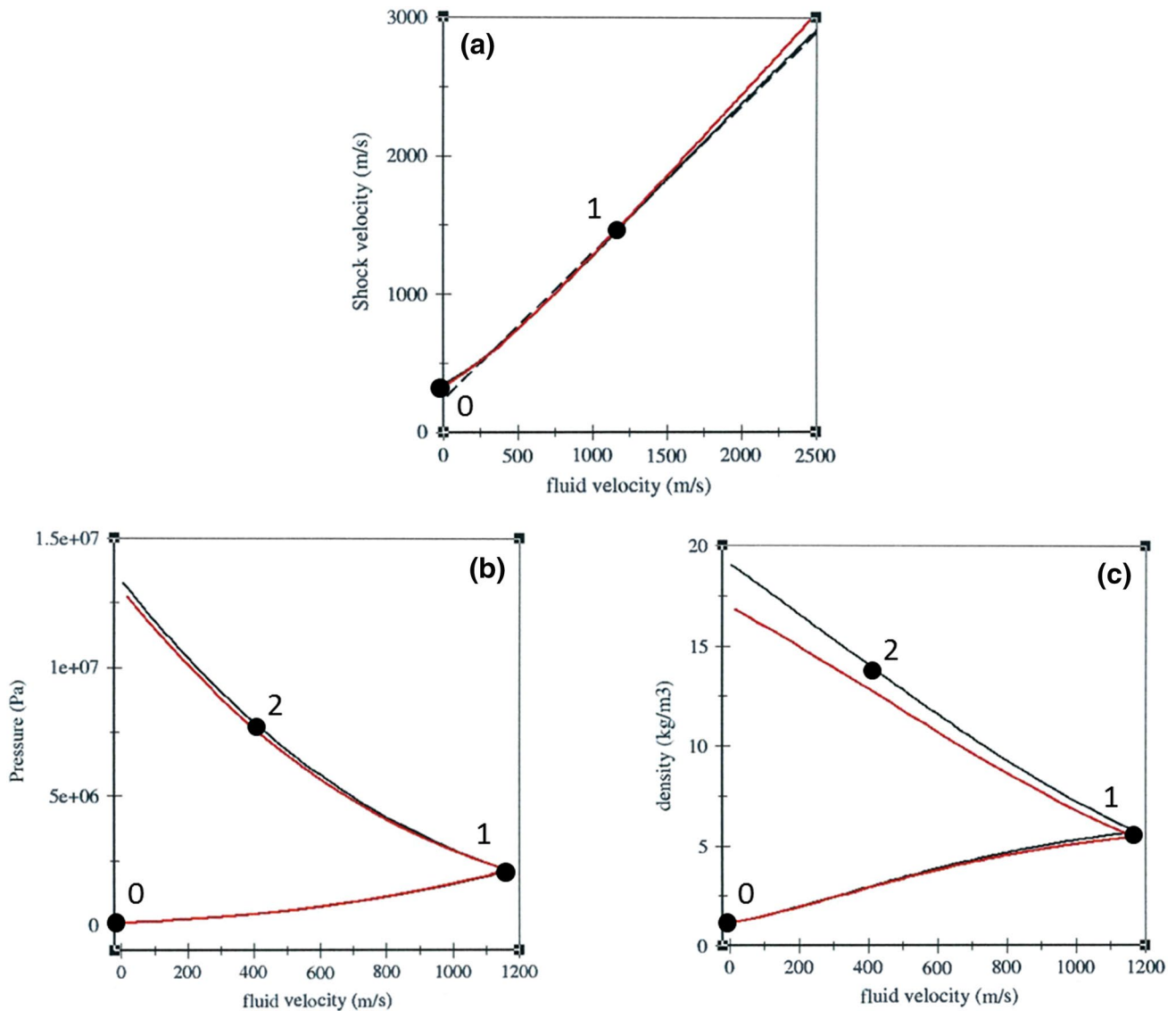


**Fig. 17** Shock properties of air subjected to a single shock (a) and to a succession of two shocks (b, c). Comparison of the SESAME 5030 equation of state for air (solid black line) with Kim's correla-

tion (dashed black line) and the perfect gas equation of state (solid red line). Points 0, 1 and 2 correspond to the initial, shocked and re-shocked states of air defined in Fig. 16

precisely what is not observable in our experiments: the liquid drop hidden by the mist.

Finally, some dedicated simulations have been performed to provide partial validation by comparison to reference cases. The results (not shown here) confirm the ability of our simulations to capture the bow shock stand-off distance [42] and the drag coefficient on a rigid sphere [39].

## 5 Simulation results and analysis

### 5.1 Comparison of the simulation with the experiments

We present in Fig. 18 the comparison between the experimental images and the simulation for Test No. 2. The accurate space and time scaling of the experimental images

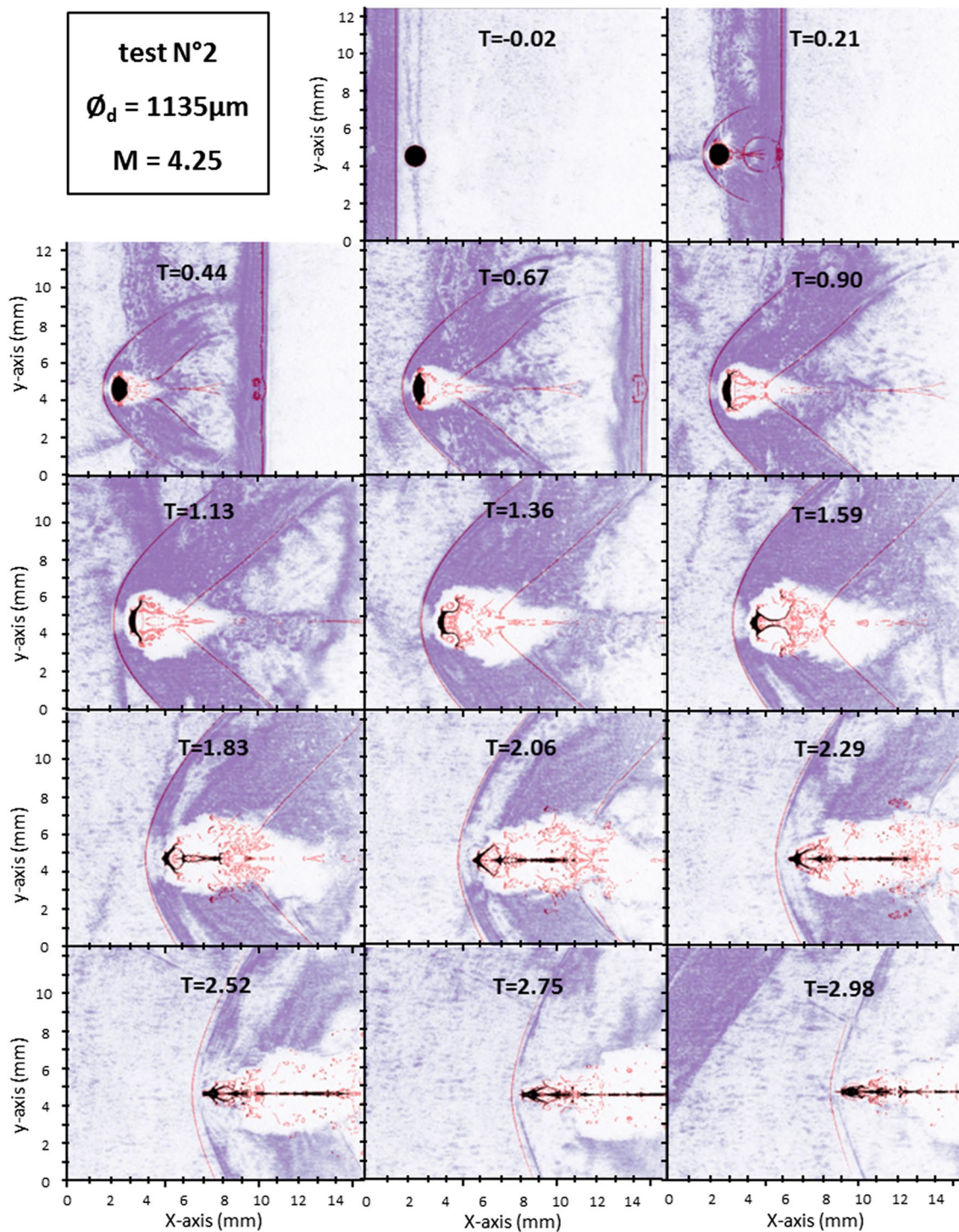


**Fig. 18** Superimposition of experiment and simulation for Test No. 2. Experimental images are displayed in shades of purple. The drop shape extracted from the simulation is shown in black and the strongest air density gradients are in red

allowed a precise superimposition. For clarity, the experimental images are converted into purple shades and the dark/light areas are inverted; i.e., the experimental drop and mist will now appear in white, whereas the drop shape extracted from the simulation is represented in black. In

order to emphasise the shock location in the simulation, the magnitude of the air density gradient is represented in red, wherever it exceeds a threshold value.

Concerning the initialisation of the simulation, the first image of Fig. 18 shows that the drop and shock positions

are satisfactorily reproduced. Moreover, if we consider the shock travelling from left to right, the three following images confirm that its velocity is very similar in the simulation and the experiment.

Considering now the full image sequence of Fig. 18, the comparison between experiment and simulation will be focused on two main observables, which are: (1) the location of the droplet inside the mist plume, and (2) the shape and location of the shock waves.

Concerning the first observable, it appears that the droplet in the simulation undergoes significant deformation and displacement as a consequence of the pressure field induced by the flow. First, the droplet evolves from its initial spherical shape to a flat, oblate spheroid. Then, part of it collapses onto the flow axis and takes the form of a filament; what remains is ejected off the axis and is fragmented into small particles. Despite this complex and coupled drop-flow evolution, we note that during the entire simulation the simulated drop is located inside the experimental mist “plume”, even the small particles generated by numerical fragmentation.

Regarding the second observable, we note that the bow shock appearing due to the supersonic flow around the droplet is well reproduced by the simulation. Its location and curvature along the  $z$  axis are in good agreement with the experimental observations. At early times, the droplet acts as a blunt body and, as noticed in Sect. 3.5, the bow shock curvature and standoff distance are directly related to the drop radius and to the relative Mach number  $M_r = (V_{m1} - V_{DSP})/c_1$ , where  $V_{DSP}$  is the velocity of the drop stagnation point (DSP). At later times, the bow shock wave turns into a conical shape, revealing that the droplet has evolved from a blunt to a sharp body. We also note that the local angle of the detached shock with the  $z$  axis (several drop diameters away from the symmetry axis) increases with time. This evolution, which is directly related to  $M_r$ , is exactly the same in the simulation and the experiment. Such agreement assumes a comparable evolution of the front part of the liquid core in both cases.

A very good agreement is also observed for the recompression shock in the wake of the droplet. Contrary to the bow shock, which is mostly sensitive to the front part of the liquid, the recompression shock is caused by the fluid circumvention around the liquid core. It is thus sensitive to the whole shape of the obstacle; i.e., its maximum cross section and its length along the flow direction. We note that the location of the wake shock in the simulation, as well as its angle, is very close to the experimental observations. More precisely, the increasing distance (along the  $z$  axis) between the bow and wake shocks appears to be a significant indication of the hydrodynamic processes occurring during the flow–drop interaction.

All of these observations suggest that the simulated flow field around the drop is very close to the experimental one throughout the entire drop deformation and breakup process. Such excellent agreement throughout the image sequence suggests that the main mechanisms responsible for the coupled evolution of the droplet and the surrounding flow are accurately captured by the hydrodynamic simulation. Consequently, we are confident to interpret the simulations more deeply, to see “through” the mist and access the droplet shape and fragmentation history.

## 5.2 Droplet displacement

As mentioned in Sect. 3.3, the experimental drop displacement curves usually describe the mist leading edge (MLE). Contrary to the experiments, the simulation yields access to the actual droplet stagnation point (DSP), and to the droplet centre of mass (DCM). The MLE, DSP and DCM displacement curves are shown in Fig. 19a (filled circles, open squares and bold solid line, respectively), along with the fit to our experimental data of MLE given by Eq. (1) with  $C_d = 2.15$  (dashed line). Also shown is the curve corresponding to the rigid sphere, i.e., Equation (1) with  $C_d = 1$  (dotted line).

At early times ( $T < 1.5$ ), Fig. 19a clearly shows that  $DSP > MLE > DCM$ . The first relation  $DSP > MLE$  corresponds to the observation already made in Fig. 18 that the drop is located inside the mist experimental zone. The second relation  $MLE > DCM$  shows that at very early times ( $T < 0.2$ ), the drop deformation is low and the DCM thus satisfies the displacement equation of a rigid sphere, i.e., Equation (1) with  $C_d = 1$ , whereas the MLE is empirically observed to satisfy Eq. (1) with  $C_d = 2.15$ . Although the simulation does not yield information on the MLE, the difference between both  $C_d$  values can be explained with a simple geometric consideration. Indeed, the drop shapes in Fig. 19b show that the leeward stagnation point of the droplet does not move at early times. If the drop remained symmetric, i.e., ellipsoidal, there would be a factor 2 between the displacements of DSP and DCM. The slight dissymmetry shown in Fig. 19b illustrates why the displacement of DSP can be described with  $C_d > 2$ .

At later times ( $T > 1.5$ ), the curves in Fig. 19a cross each other and  $DCM > MLE \sim DSP$ . The relation  $MLE \sim DSP$  is consistent with the drastic change in the droplet shape, previously assimilated to a sharp body (see Sect. 5.1). Similarly, the droplet deformation also explains that the DCM becomes located much further, as shown in Fig. 19c. The analysis of the changes in the droplet shape will be discussed in the next section.

Looking accurately at the results, it is also interesting to notice that the DCM does not follow the constant



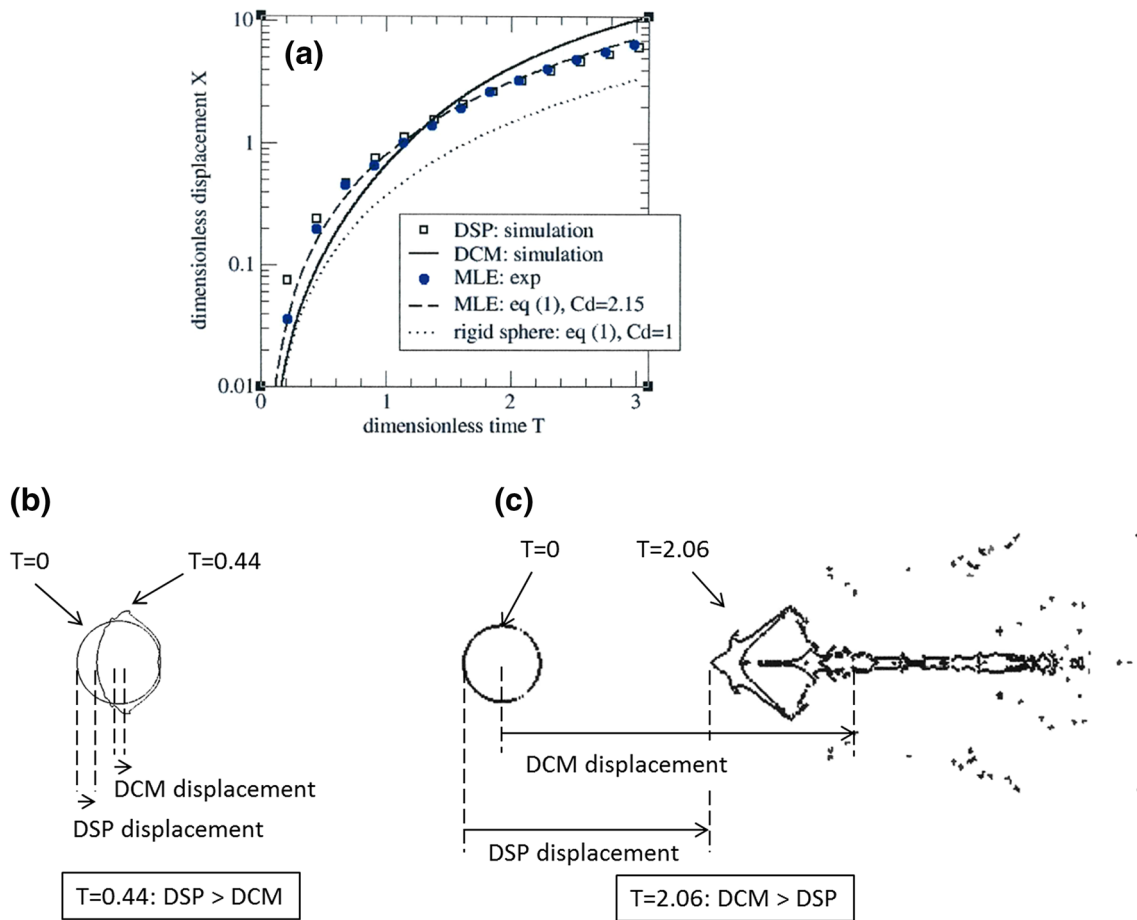


**Fig. 19** Dimensionless displacement  $X$  as a function of dimensionless time (a), and drop deformation at **b** early and **c** late times, showing drop stagnation point (DSP) and drop centre of mass (DCM) displacements

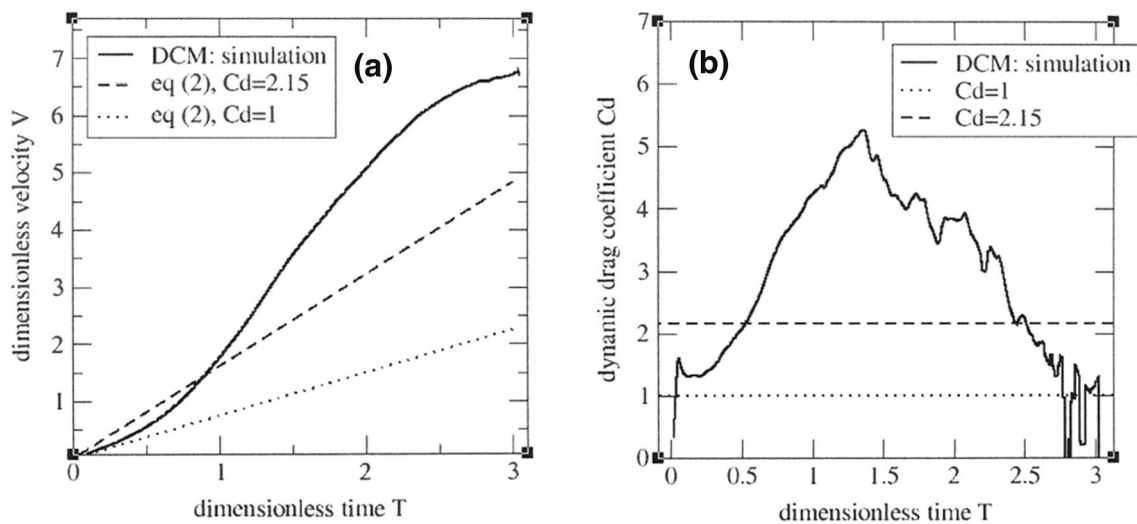


**Fig. 20** Evolution of dimensionless velocity and the dynamic drag coefficient as a function of time

acceleration equation observed for MLE. This is illustrated in Fig. 20a, where the velocity evolution of the DCM (solid bold line) and MLE (dashed line) are compared in dimensionless scales defined as follow. Noting the velocity as  $v$ , the dimensionless velocity  $V$  is defined by  $V = \frac{v}{v_c} = \frac{dx}{dT}$  with  $v_c = \varnothing_d/t_c = V_{m1} (\rho_1/\rho_d)^{1/2}$ . Thus, following Eq. (1), the dimensionless MLE velocity increases linearly with the dimensionless time:

$$V = \frac{v}{v_c} = \frac{3}{4} C_d T \quad (2)$$

We recall that this equation, which corresponds to a constant acceleration, is usually related to the hypothesis of a rigid body without deformation or mass loss, and having a negligible velocity compared to the upstream fluid. Equation (2) is represented by a straight line in Fig. 20a. At early times ( $T < 0.2$ ), as long as the drop remains roughly spherical, it is observed that the DCM follows Eq. (2) with  $C_d = 1$ . Then, due to the drop shape evolution, the DCM velocity clearly deviates from this ideal behaviour.

In order to analyse how the drop deformation affects the dynamic drag coefficient  $C_d$ , the evolution of the latter is deduced from the following relation:

$$C_d = \frac{4}{3} \frac{dV}{dT} \quad (3)$$

Figure 20b shows the strong difference between the effective drag coefficient  $C_d = 2.15$  deduced from the MLE position, and the actual dynamic drag coefficient corresponding to the DCM. At early times ( $T < 0.2$ ), the latter begins with a transitory peak above 1 followed by a decrease, an evolution consistent with other published data on rigid spheres under similar conditions [7, 48–50]. However, at later times the dynamic drag coefficient dramatically increases until it reaches the value  $C_d \sim 5$  at  $T \sim 1.5$ . Then, a strong decrease is observed, until  $T \sim 3$  where  $C_d$  is close to 1. In Fig. 20b are also plotted the constant values  $C_d = 1$  corresponding to the stationary value for a sphere. The variation of  $C_d$  is obviously related to the drop deformation. For instance, it is known that the drag coefficient of an oblate (resp., prolate) spheroid is greater (resp., smaller) than that of a sphere.

Similar observations can be found in [27], but with the maximum drag occurring a bit earlier ( $T \sim 0.75$ ). However, these simulations correspond to lower Mach numbers (1.18–1.73). Other simulations by the same author [27] at Mach 2.00 and 2.50 do not clearly show the decrease of  $C_d$ , but these simulations were limited to  $T < 1.5$ . It is interesting to refer also to the simulation results of Kekesi [21], where the maximum  $C_d$  appears at  $T \sim 4$ ; however, his study concerned very low Weber numbers ( $W_e < 12$ ). Finally, this

discussion suggests that the peak value of the dynamic drag coefficient depends on some physical parameters, which may be the Mach or Weber number. The possible effect of the numerical methods used for the simulations should also be investigated.

### 5.3 Droplet deformation

The discussion of Sect. 5.2 has emphasised the dominant role played by drop deformation in the observations. We now use the simulation to discuss the phenomenology of droplet deformation and fragmentation.

The droplet deformation extracted from the simulations has already been shown in Fig. 18. It is now reproduced in Fig. 21, where we distinguish 3 steps:

- $T < 1$  (Fig. 21a): according to the simulation, the liquid mass remains in one main drop, whose shape flattens due to the aerodynamic forces. Indeed, the aerodynamic pressure on the drop surface is maximum at the stagnation point and decreases at higher radius. The resulting hydrodynamic phenomenon (radial expansion of the liquid) has been already identified by Burgers and Reinecke in their deformation models [41]. Another validation of our simulations comes from the X-ray observations made by Reinecke in similar conditions [15]. This deformation is associated with the increase in  $C_d$  related to DCM (Fig. 19c), leading to a strong acceleration that can drive Rayleigh–Taylor (RT) instability on the windward surface of the drop [9]. The simulation does not capture the initial mist generation shown in Fig. 5. However, the corresponding mass loss is small [4, 12, 23, 40, 51], and its effect on the subsequent hydrodynamic processes can be neglected.
- $1 < T < 2$  (Fig. 21b): at later times, two hydrodynamic phenomena appear to be in competition. First, we observe that large amplitude oscillations appear on the windward surface of the drop at  $T = 1.38$  and  $T = 1.61$ , which may be due to RT instability. However, their growth seems to be dominated by another hydrodynamic phenomenon, which is the radial motion of the liquid. Indeed, the simulation suggests that the outer rim of the liquid drop splits into two parts; the first one collapses onto the axis and the other one spreads out radially in small fragments. We note that a possible explanation of this splitting comes from the fact that, in a supersonic flow, the aerodynamic force acting on a small fragment close to a bigger one can lead either to separation or to “collimation” of the former in the trail of the latter [52]. The mass included in the outer rim is significant ( $\sim 50\%$  of the total mass), which explains why its relative acceleration during the first half of this

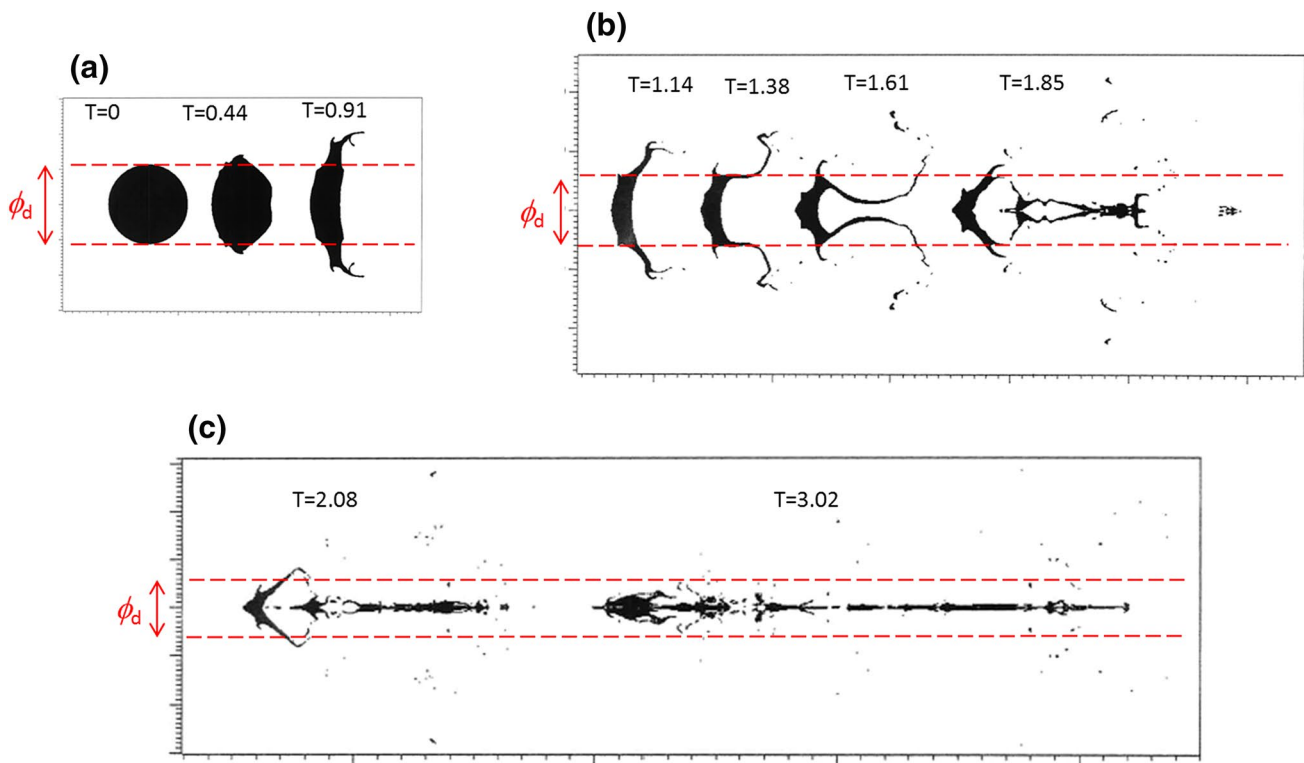


**Fig. 21** Droplet deformation. In order to facilitate comparison between all drop shapes, dashed red lines have been added to materialise the initial drop diameter. Positions along the x-axis are arbitrary to facilitate visualisation

step ( $1 < T < 1.5$ ) leads to an increase in  $C_d$  (DCM), as observed in Fig. 19c. Then, the decrease of  $C_d$  during the second half of this step ( $1.5 < T < 2$ ) is due to two mechanisms: first, the evolution of the global shape of the liquid remains, which tends to concentrate on the flow axis; and second, the small fragments equilibrate with the fluid velocity and do not accelerate anymore.

- $2 < T < 3$  (Fig. 21c): Finally, the drop takes the shape of a liquid filament, aligned with the flow. The axial spreading becomes significant, leading to an aspect ratio much different from 1, which explains the decreasing  $C_d$ .

In order to discuss these results more quantitatively, we will now define the parameter  $R$ , which is the radial extension of the drop in the simulation. For simplicity, we define  $R$  as the maximum radius of the cells where the volume fraction of liquid is greater than 99%. The evolution of  $R$  can be compared to the experimental measurement of the drop radial deformation. These values are plotted on dimensionless scales in Fig. 22. Simulation and experiment follow a similar evolution, despite a quantitative difference. More precisely, for  $T < 1.5$ , both quantities increase with time, and the difference is attributed to the mist. For  $T > 1.5$ , the large experimental radius (not considering the

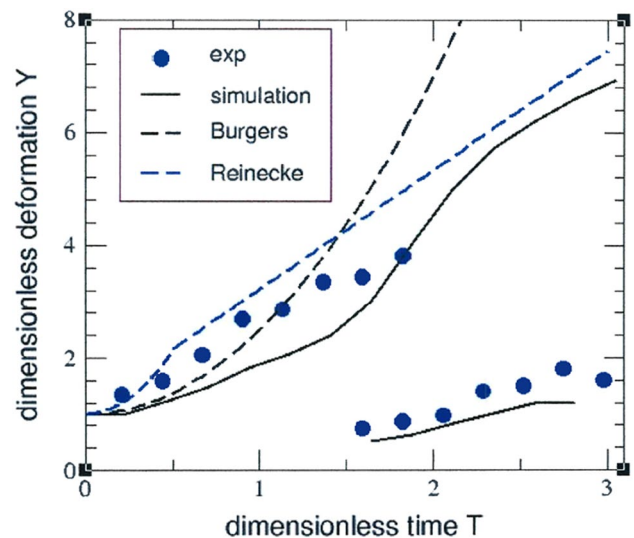


**Fig. 22** Dimensionless deformation as a function of dimensionless time  $T$ . Experimental data are taken from Test No. 2 in Fig. 10

“tip”) becomes difficult to define, and this comparison cannot be made any longer.

Figure 22, also includes the Burgers and Reinecke models [41] for drop deformation. It appears that the latter,

by construction, follows the deformation as indicated by mist, whereas the former is in better agreement with our simulations. In fact, the Reinecke model assumes that the drop windward surface is flat and experiences a homogeneous pressure, whereas Burgers made the hypothesis of a spherical drop with a cosine-shaped pressure field. The drop shapes shown in Fig. 21a suggest that the Burgers model may be more appropriate for  $T < 0.5$ . At later times  $T = 0.91$ , the deformation predicted by the Burgers model is overestimated because it neglects the shear induced longitudinal entrainment (SIE) of the liquid at the periphery of the drop, which limits its radial expansion both in our simulations and in the experiment.

Finally, for  $T > 1.5$ , we have extracted from the simulation the radius of the “tip” and compared it to the experimental data. A good agreement is also observed for this particular pattern, which suggests that our simulation provides an accurate description of the liquid core deformation.

Beyond the quantitative results, an important conclusion of this study is the phenomenology deduced from the drop deformation analysis. Indeed, the fact that the drop evolves to a filament shape extending along the flow axis is a new result. We note that it has some similarities with the ‘bag and stamen’ breakup mechanism observed at much lower Weber numbers. An important consequence is that such a filament, if real, could not have been resolved with the X-ray diagnostics used by Reinecke to see ‘through’ the mist, and which led him to diminish his total breakup time estimate [15, 19]. However, the mass

contained in this filament is far from negligible, as will be discussed in Sect. 5.6.

### 5.4 Bow shock standoff distance

From the simulation, we extract the distance between the bow shock and the DSP. These values are shown in Fig. 23 along with the experimental data corresponding to the distance between the bow shock and the MLE. A similar evolution is observed, as well as a quantitative difference which we interpret as the thickness of the mist layer in front of the droplet. Thus, under the conditions studied here, the leading edge of the droplet (DSP) is 30% further from the bow shock than the MLE. Although we do not have a definitive explanation for this observation, it is noteworthy that the air flow at the front face of the droplet is subsonic. It is thus possible that the hydrodynamic instabilities appearing at the drop surface may lead to turbulent mixing that could be responsible for the 30% extension of the mist between the drop and the bow shock. Additional experiments with more precise diagnostics, such as Laser Induced Fluorescence (LIF), could provide valuable information on this question.

Despite this difference, we can use the simulation results to analyse the relative importance of the two effects (drop diameter and relative velocity) that drive the evolution of the shock layer thickness. The following relation, initially proposed by Billig [42], gives the shock standoff distance  $\delta$  for a rigid sphere of diameter  $D$  in air flowing at a relative Mach number  $M$ :

$$\frac{\delta}{D} = 0.0715 \exp\left(\frac{3.24}{M^2}\right) \tag{4}$$

After logarithmic derivation, it yields:

$$\frac{d\delta}{\delta} = \frac{dD}{D} - 6.48 \frac{dM}{M^3} \tag{5}$$

In order to use this equation to interpret our data, we note that  $d\delta/\delta$  and  $dD/D$  from Eq. (5) correspond to  $dB/B$  and  $dY/Y$ , respectively. Thus, with our notations, Billig’s relation leads to:

$$\frac{dB}{B} = \frac{dY}{Y} - 6.48 \frac{dM}{M^3} \tag{6}$$

The first term of the right hand side of Eq. (6) is thus estimated from the simulated deformation  $Y$  shown in Fig. 22. Considering the evolution between  $T = 0$  and  $T = 1.5$ , we find  $dY/Y \sim 1.5$ . Then, the Mach variation due drop acceleration is estimated using Eq. (2): between  $T = 0$  and  $T = 1.5$ ,  $dV = 9 \cdot C_d/8$ , leading to  $dM = -v_c \cdot dV/c_1 = -(9 \cdot C_d/8) \cdot (V_{m1}/c_1) \cdot (\rho_1/\rho_d)^{1/2}$ . Under our conditions, we have  $M = V_{m1}/c_1 \sim 1.6$  and  $dM \sim -0.3$ , so

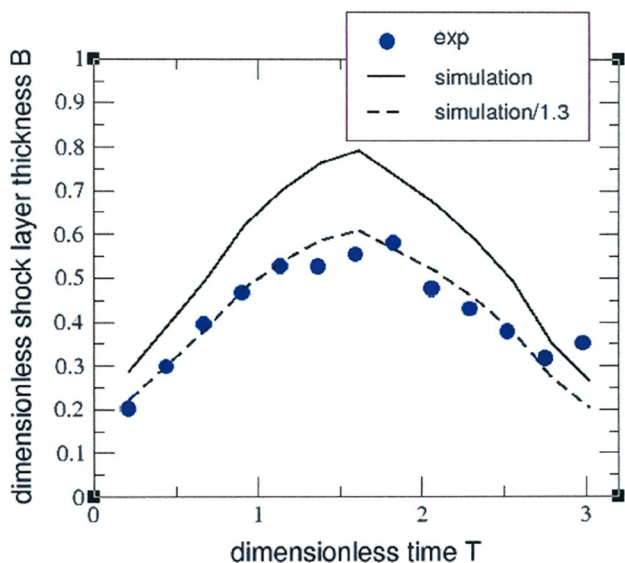


Fig. 23 Dimensionless shock layer thickness as a function of dimensionless time  $T$ . Experimental data are taken from Test No. 2 in Fig. 12

the second term on the right hand side of Eq. (6) roughly equals 0.5. Thus, Eq. (6) predicts  $dB/B \sim 2$ , which means a 200% increase in the shock standoff distance between  $T=0$  and  $T=1.5$ . This estimate is in good agreement with Fig. 23. Obviously, some error comes from the fact that Eq. (4) is not strictly valid, since the drop does not remain spherical. However, this simple model allows us to conclude that the major cause of the increase observed in Fig. 23 between  $T=0$  and  $T=1.5$  is drop deformation, and that drop acceleration is of much less importance. At times  $T > 1.5$ , the windward face of the drop is strongly modified because of the appearance of a prominent tip, and Billig's relation cannot provide quantitative information for such a complicated shape. However, qualitatively, it suggests that the decrease in  $B$  is likely to be due to the small radius of curvature at the tip front end. Finally, the present analysis shows that the shock standoff distance can provide useful information on the shape of the liquid core facing the flow.

### 5.5 Distance between bow and wake shocks

The dimensionless distance  $W$  between the bow and wake shocks has been extracted from the simulation at the same distance from the axis (5 drop initial radii) as in the experiments. The comparison is shown in Fig. 24. Simulation and experiment show a very similar evolution, consisting in a continuous increase linked to the drop deformation. However, it is noteworthy that the previous observables (drag coefficient  $C_d$ , deformation  $Y$ , shock standoff distance  $B$ ) showed a clear change around  $T=1.5$ . It is not the case here, which could seem surprising. Indeed, our simulations suggest that, at  $T < 1.5$ , the increase in  $W$  is due to

the flattening of the drop, and that at  $T > 1.5$  it is due to the more elongated shape shown in Fig. 21. The simulations shown here suggest that  $W$  is somewhat less sensitive to the aspect ratio of the droplet than  $C_d$ ,  $Y$  and  $B$ . Further investigation of this question will be addressed in future work.

### 5.6 Droplet remaining mass

In this section, we will use our simulation results to compute the evolution of the mass contained in the main central fragment. Indeed, usual models for droplet fragmentation rely on a description of the evolution of the droplet mass [23, 40, 53]. From his experimental data in the high Weber ('catastrophic') regime, Reinecke [15] proposed the following empirical correlation:

$$\frac{m}{m_0} = \frac{1}{2} \left( 1 + \cos \left( \frac{\pi \cdot T}{T_b} \right) \right) \tag{7}$$

where  $m_0$  is the initial drop mass and  $m$  is the remaining mass at dimensionless time  $T$ . Reinecke [15] also suggests that the dimensionless time for complete breakup  $T_b$  can be estimated with the following relation:

$$T_b = 45 \cdot W_e^{-1/4} \tag{8}$$

Under the conditions of our Experiment No. 2, Eq. (8) gives  $T_b \sim 2.4$  and the above model is plotted in Fig. 25 (dashed line).

In a recent paper [22], the remaining mass in the liquid core was extracted from a numerical simulation, with the assumption that it is equal to the amount of liquid

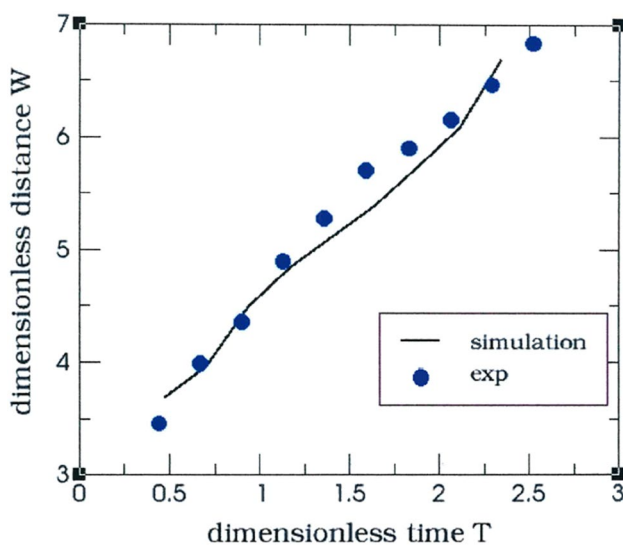


Fig. 24 Evolution of distance between the bow and wake shocks. Experimental data are taken from Test No. 2 in Fig. 14

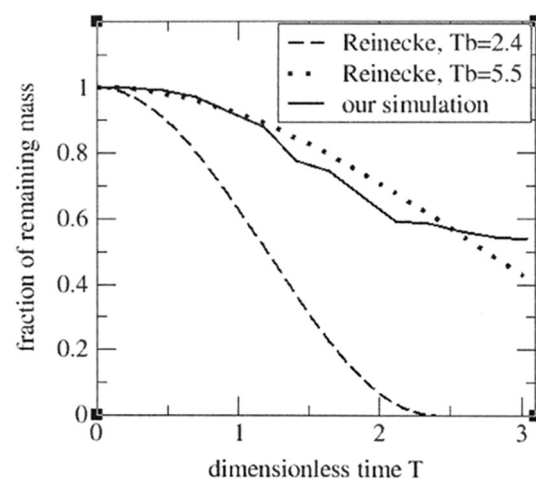


Fig. 25 Evolution of mass fraction of the liquid pure mesh (solid line) and comparison with the Reinecke model Eq. (7), where the total breakup time  $T_b$  is either calculated from Eq. (8) (dashed line) or equal to 5.5 (dotted line)

remaining in pure cells. Using the same methodology, the mass in the cells where the volume fraction of liquid is greater than 99% was extracted from our simulation at different times, and divided by the initial mass of the drop. The resulting curve is presented in Fig. 25 (solid line). We observe that more than 50% of the initial liquid mass remains in the liquid core at the end of our simulation ( $T \sim 3$ ), which is in disagreement with Eq. (8). As discussed in Sect. 5.4, the reason for this discrepancy probably comes from a lack of resolution of Reinecke's X-ray diagnostic tool when the drop shape evolves into a filament, and we suspect that Eq. (8) actually underestimates  $T_b$ . Indeed, we also show in Fig. 25 (dotted line) that using the value  $T_b = 5.5$  suggested by Pilch [4] leads to a much better agreement between Eq. (7) and our simulation.

Finally, we note that this higher value is consistent with our experimental observations. Indeed, although they do not provide a direct estimation of the breakup time, the presence of a bow shock (visible in Fig. 9 for instance) suggests that  $T_b > 3$ .

## 6 Conclusion

We have presented new experiments of breakup of water droplet at Weber number above  $10^5$ . We used high resolution ombroscopy with precise temporal synchronisation. 16 images were available per shot, which helped in limiting shot-to-shot variations of the initial conditions. Our experimental results show a very good repeatability and we have extracted much quantitative information, such as drop displacement and deformation. Moreover, the locations of the bow and wake shocks in the air flow around the droplet have also been analysed, and it has been observed that all of these quantities scale fairly well with the initial drop diameter.

Numerical hydrodynamic simulations have also been presented. Extensive comparisons with experimental data show a very good agreement and allow the deformation and fragmentation mechanisms of the water droplet to be analysed more precisely. According to our results, the deformation mechanism can be divided into 3 steps. First, at  $T < 1$ , most of the liquid mass remains in one main drop, whose shape flattens due to the hydrodynamic forces; then, at  $1 < T < 2$ , fragmentation begins along the outer rim of the liquid drop and splits the corresponding mass into two parts; the first one collapses onto the axis and the other one spreads out radially in small fragments. The mass included in the outer rim is approximately half of the total mass. Finally for  $2 < T < 3.5$ , the remaining liquid mass takes the shape of a filament, aligned with the flow.

We emphasise that our experimental and numerical results are consistent with a complete breakup time

$T_b = 5.5$ , as suggested by [4]. Further experiments with observations at  $T > 4$  will be performed soon to confirm this value. Moreover, it appears that complementary diagnostics, such as Laser Induced Fluorescence, could be appropriate to see 'through the mist' and validate the present analysis.

**Acknowledgements** The authors want to thank Pr. Philippe Villedieu for fruitful discussions on the experimental data as well as the simulation results.

## Compliance with ethical standards

**Conflict of interest** On behalf of all authors, the corresponding author states that there is no conflict of interest.

## References

1. Turner MR, Sazhin SS, Healey JJ, Crua C, Martynov SB (2012) A breakup model for transient Diesel fuel sprays. *Fuel* 97:288–305
2. Kindracki J (2015) Experimental research on rotating detonation in liquid fuel–gaseous air mixtures. *Aerosp Sci Technol* 43:445–453
3. Chauvin A, Jourdan G, Daniel E, Houas L, Tosello R (2011) Experimental investigation of the propagation of a planar shock wave through a two-phase gas–liquid medium. *Phys Fluids* 23(11):113301
4. Pilch M, Erdman CA (1987) Use of breakup time data and velocity history data to predict the maximum size of stable fragments for acceleration-induced breakup of a liquid drop. *Int J Multiphase Flow* 13(6):741–757
5. Chauvin A, Daniel E, Chinnayya A, Massoni J, Jourdan G (2016) Shock waves in sprays: numerical study of secondary atomization and experimental comparison. *Shock Waves* 26(4):403–415
6. O'Rourke PJ (1981) Collective drop effects on vaporizing liquid sprays. Ph.D. thesis, Princeton University
7. Ling Y, Haselbacher A, Balachandar S, Najjar FM, Stewart DS (2013) Shock interaction with deformable particle: direct numerical simulation and point-particle modeling. *J Appl Phys* 113(1):013504
8. Marois G (2018) Modélisation eulérienne de l'interaction d'un brouillard avec un choc en régime supersonique. Ph.D. thesis, Université de Toulouse
9. Pilch M (1981) Acceleration induced fragmentation of liquid drops. Ph.D. thesis, University of Virginia
10. Gelfand BE (1996) Droplet breakup phenomena in flows with velocity lag. *Prog Energy Combust Sci* 22:201–265
11. Guildenbecher DR, Lopez-Rivera C, Sojka PE (2009) Secondary atomization. *Exp Fluids* 46(3):371–402
12. Theofanous TG, Li GJ (2008) On the physics of aerobreakup. *Phys Fluids* 20:052103
13. Theofanous TG, Li GJ, Dinh TN (2004) Aerobreakup in rarefied supersonic gas flows. *Trans ASME* 126:516–527
14. Ranger AA, Nicholls JA (1972) Atomization of liquid droplets in a convective gas stream. *Int J Heat Mass Transf* 15:1203–1211
15. Reinecke WG, Waldman GD (1970) An investigation of water drop disintegration in the region behind strong shock waves. In: 3rd International conference on rain erosion and related phenomena, Hampshire, England
16. Wierzbka A, Takayama K (1988) Experimental investigation of the aerodynamic breakup of liquid drops. *AIAA J* 26(11):1329–1335

17. Simpkins PG, Bales EL (1972) Water-drop response to sudden accelerations. *J. Fluid Mech* 55(4):629–639
18. Joseph DD, Belanger J, Beavers GS (1999) Breakup of a liquid drop suddenly exposed to a high-speed airstream. *Int J Multiph Flow* 25:1263–1303
19. Reinecke WG, McKay WL (1969) Experiments on water drop breakup behind Mach 3 to 12 shocks. Report SC-CR-70-6063
20. Khosla S, Smith CE, Throckmorton RP (2006) Detailed understanding of drop atomization by gas crossflow using the volume of fluid method. In: ILASS Americas, 19th annual conference on liquid atomization and spray systems, Toronto, Canada, May 2006
21. Kékesi T, Amberg G, Prah Wittberg L (2014) Drop deformation and breakup. *Int J Multiph Flow* 66:1–10
22. Liu N, Wang Z, Sun M, Wang H, Wang B (2018) Numerical simulation of liquid droplet breakup in supersonic flows. *Acta Astronaut* 145:116–130
23. Chou WH, Hsiang LP, Faeth GM (1997) Temporal properties of drop breakup in the shear breakup regime. *Int J Multiph Flows* 23(4):651–669
24. Chang C, Deng X, Theofanous T (2013) Direct numerical simulation of interfacial instabilities: a consistent, conservative, all-speed, sharp-interface method. *J Comput Phys* 242:946–990
25. Zaleski S, Li J, Succi S (1995) Two-dimensional Navier-Stokes simulation of deformation and breakup of liquid patches. *Phys Rev Lett* 75(2):244–247
26. Aalburg C, van Leer B, Faeth MG (2003) Deformation and drag properties of round drops subjected to shock-wave disturbances. *AIAA J* 41:2371–2378
27. Meng JC, Colonius T (2015) Numerical simulations of the early stages of high-speed droplet breakup. *Shock Waves* 25:399–414
28. Meng JC, Colonius T (2018) Numerical simulation of the aerobreakup of a water droplet. *J Fluid Mech* 835:1108–1135
29. Igra D, Takayama K (2001) Numerical simulation of shock wave interaction with a water column. *Shock Waves* 11:219–228
30. Wang T, Liu N, Yi X, Lu X, Wang P (2018) Numerical study on shock/droplet interaction before a standingwall. *Commun Comput Phys* 23(4):1052–1077
31. Chen H, Liang SM (2008) Flow visualization of shock/water column interactions. *Shock Waves* 17:309–321
32. Igra D, Takayama K (1999) Investigation of aerodynamic breakup of a cylindrical water droplet. *Rep Inst Fluid Sci Tohoku Univ* 11:123–134
33. Sembian S, Liverts M, Tillmark N, Apazidis N (2016) Plane shock wave interaction with a cylindrical water column. *Phys Fluids* 28:056102
34. Guan B, Liu Y, Wen C-Y, Shen H (2018) Numerical study on liquid droplet internal flow under shock impact. *AIAA J* 56(9):3382–3387
35. Lee BHK (1967) Detonation-driven shocks in a shock tube. *AIAA J* 5(4):791–792
36. Zhao W, Jiang ZL, Saito T, Lin JM, Yu HR, Takayama K (2005) Performance of a detonation driven shock tunnel. *Shock Waves* 14(1–2):53–59
37. Kim IH, Hong SH, Jhung KS, Oh K-H, Yoon YK (1991) Relationship among shock-wave velocity, particle velocity, and adiabatic exponent for dry air. *J Appl Phys* 70(2):1048–1050
38. Zel'dovich YB, Raizer YP (1966) *Physics of shock waves and high-temperature hydrodynamic phenomena*. Academic Press, New York
39. Anderson JD Jr (2006) *Hypersonic and high-temperature gas dynamics*, AIAA education series, 2nd edn. AIAA, Reston
40. Ranger AA, Nicholls JA (1969) Aerodynamic shattering of liquid drops. *AIAA J* 7(2):285–290
41. Reinecke WG, Waldman GD (1975) Shock layer shattering of cloud drops in reentry flight. AIAA paper 75-152, AIAA 13th Aerospace Science meeting
42. Billig FS (1967) Shockwave shapes around spherical and cylindrical nosed bodies. *J Spacecr Rockets* 4(6):822–823
43. Hébert D, Seisson G, Rullier J-L, Bertron I, Hallo L, Chevalier J-M, Thessieux C, Guillet F, Boustie M, Berthe L (2017) Hypervelocity impacts into porous graphite: experiments and simulations. *Philos Trans R Soc A* 375:20160171
44. Osher S (1989) The nonconvex multidimensional Riemann problem for Hamilton–Jacobi equations. NASA Contractor Report 181887, ICASE report No. 89-53
45. Mosso S, Clancy S (1995) A geometrically derived priority system for Young's interface reconstruction. Technical report LA-CP-95-0081, Los Alamos National Laboratory
46. Zamishlyayev BV, Menzhulin MG (1971) Interpolation equation of state of water and water vapor. *Zh Prikl Mek Tek Fiz* 3:113–118
47. Lyon SP, Johnson JD (1992) SESAME: the Los Alamos National Laboratory equation of state database. LA-UR-92-3407
48. Tanno H, Itoh K, Saito T, Abe A, Takayama K (2003) Interaction of a shock with a sphere suspended in a vertical shock tube. *Shock Waves* 13:191–200
49. Parmar M, Haselbacher A, Balachandar S (2009) Modeling of the unsteady force for shock-particle interaction. *Shock Waves* 19(4):317–329
50. Mehta Y, Jackson TL, Zhang J, Balachandar S (2016) Numerical investigation of shock interaction with one-dimensional transverse array of particles in air. *J Appl Phys* 119:104901
51. Girin OG (2014) A model of an atomizing drop. *At Sprays* 24(11):977–997
52. Barri NG (2010) Meteoroid fragments dynamics: collimation effect. *Sol Syst Res* 44(1):55–59
53. Reinecke WG, Waldman GD, McKay WL (1979) A general correlation of flow-induced drop acceleration, deformation and shattering. In: 5th international conference on erosion by liquid and solid impact

**Publisher's Note** Springer Nature remains neutral with regard to jurisdictional claims in published maps and institutional affiliations.